Title

Symmetry Dictated Properties in Two-dimensional Systems

Author

Yang, Fuyi

Publication Date

2022

Peer reviewed|Thesis/dissertation

Symmetry Dictated Properties in Two-dimensional Systems

By

Fuyi Yang

A dissertation submitted in partial satisfaction of the

requirements for the degree of

Doctor of Philosophy

in

Engineering – Materials Science and Engineering

in the

Graduate Division

of the

University of California, Berkeley

Committee in charge:

Professor Jie Yao, Chair

Professor Jeffrey Bokor

Professor Junqiao Wu

Spring 2022

Abstract

Symmetry Dictated Properties in Two-dimensional Systems

by

Fuyi Yang

Doctor of Philosophy in Materials Science and Engineering

University of California, Berkeley

Professor Jie Yao, Chair

The physical properties of crystalized materials are closely related to the symmetry elements of the point group of the crystal. To the contrary, engineered symmetry breaking would allow the emergence of new physical phenomena which are originally forbidden. With the successful exfoliation of two-dimensional Van der Waals materials, the restricted stacking sequence between layers is relaxed and thus, the symmetry of artificially stacked heterostructure can be readily controlled.

In this dissertation, we present two approaches to engineer the symmetry of solid-state and photonic two-dimensional systems respectively. The resulting optical and topological property changes are explored and related back to the underlying symmetry breaking. Chapter 1 gives an overview of the various symmetry breaking mechanisms and their distinct consequences. The emphasis is given to the inversion-symmetry breaking which can be easily implemented in two-dimensional systems via structural or electrical means. In Chapter 2, we show that introducing a twisting between two layers of graphene, the symmetry of bilayer structure is decisively changed, and new nonlinear optical effects are allowable. We further verify that the observed nonlinear signals are controlled by the composited bilayer instead of the linear combination of two individual layers experimentally and confirmed by DFT calculations. The methodology proposed is generic and can be applied to other composite systems. In Chapter 3, we break the symmetry of two-dimensional photonic lattice by 'tilting' the constitutive parameter tensors and demonstrate spin degeneracy lifting via electromagnetic simulations. The approach allows us to enlarge the scale of spin-orbit coupling effect in a photonic platform and at the same time, the controllability of spin-polarized energy bands associated with symmetry is revealed.

To sum up, we propose two methods to engineer the symmetry of the 2D system in a controllable way and show their potential for new physical properties and applications.

Table of Contents

Acknowledgements

First and foremost, I would like to express my sincere gratitude to my supervisor, Professor Jie Yao, who mentored me with continuous support for the last five years. His insightful suggestions and ambition for science inspired and encouraged me all the time of my academic research and daily life. I would also like to thank all the members I worked with in the Yao group. It is their kind help and support that have made my study in Berkeley enjoyable and fulfilling.

My gratitude extends to all my collaborators: Professor Li Yang and Dr. Wenshen Song from Washington University, Dr. Edward Bernard and Dr. Emory Chan from Lawrence Berkeley National Laboratory. It will not be possible to complete my project without their immense knowledge and constructive advice.

I would like to thank all the members of my committee: Professor Junqiao Wu, Professor Jeffrey Bokor, Professor Mark Asta and Professor Lane Martin for their support with my qualification exam and the preparation of dissertation.

Finally, I am deeply grateful to my parents and grandparents for their tremendous understanding and encouragement.

Chapter 1: Introduction

1.1 Symmetry breaking in two-dimensional materials

Since the first successful exfoliation of monolayer graphene, studies expand from its intrinsic low-dimensional properties to more intriguing homostructured and heterostructured stacks. Due to the relaxed Van der Waals bonding and nonnegligible coupling between layers, new types of 'composite materials' made of different Van der Waals constituents are predicted to hold new physics which are not present in their naturally stacked structures[1–4]. The unprecedented capability in manipulating the symmetry while maintaining the single crystallinity has enabled recent discoveries of superconductivity, correlated electron state, Chern insulator, ferromagnetism and more exotic physical phenomena in this low-dimensional platform[5–8]. Different stacking sequence, stacking angle or external stimuli such as doping or gating applied to achieve the desired property are fundamentally related to the symmetry breaking in these 'composite materials'.

One of the most common symmetry breaking scenarios is inversion-symmetry breaking[9]. A vertical electric field can effectively achieve the effect by shifting the on-site potential of two layers by $\pm\Delta$ as shown in the insert of Figure 1.1. For the originally centrosymmetric bilayer structure, vertical electric field not only modify the energy dispersion, but also permits valley Hall effect due to the existence of finite local Berry curvature and even order of nonlinear effects[10–13]. The direct link between the magnitude of electric field and the degree of inversion symmetry breaking further indicate the possibility of flexible tuning[14,15].

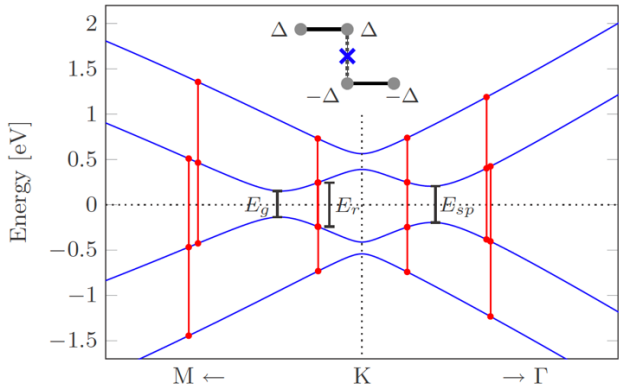

Figure 1.1 Band structure of a biased bilayer graphene (BLG) near the K point. The inset shows the four-atom unit cell of BLG with shifted on-site potentials. The blue cross marks the inversion point when the electric field is zero. Figure adapted from[13].

Breaking the sublattice symmetry in each unit cell is equivalent to the breaking of inversion symmetry of the whole structure[16]. Thus, placing monolayer graphene right on top of h-BN with atoms aligned with each other differentiate the on-site potential of two sublattices. Like the vertical electric field case, originally forbidden phenomena such as, valley Hall effect and nonlinear effect are now allowed[17–19]. This strategy has also been widely adopted to break the inversion symmetry in two-dimensional honeycomb photonic systems and stimulates photonic valley Hall studies (Figure 1.2)[20,21]. By assigning different refractive index to two sublattices, a gap will open at K and K' points with modes carrying opposite orbital angular moment (OAM) and local berry

curvature values (Figure 1.2c and 1.2d). Observation of OAM generation and kink states in the valley gaps confirms the efficacy of staggered potential in breaking the inversion symmetry[21–23].

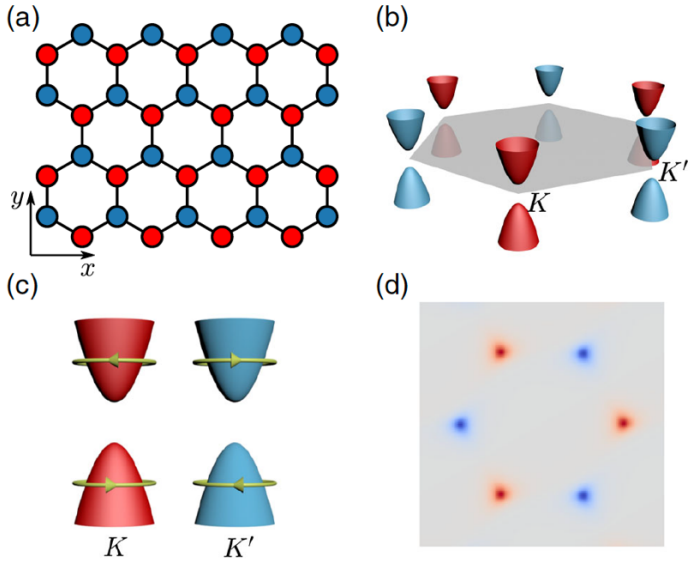

Figure 1.2 (a) A honeycomb lattice with only nearest-neighbor coupling. The red and blue sites have different on-site energies. (b) Illustration of massive Dirac cones located at the corners of Brillouin zone. (c) The Bloch states at opposite valleys exhibit opposite self-rotating direction, as indicated by the yellow arrows. (d) Berry curvature distribution. Figure adapted from[21].

Besides in-plane translational shifting, relative twisting between layers dramatically changes the symmetry elements of the 'composite' system[24–29]. Under certain conditions, the inversion symmetry is also broken and lead to twist-angle dependent phenomena which will be elaborated in Chapter 2.

It is also common for Van der Waals materials to possess C_3 or C_6 rotational symmetry and time-reversal symmetry. The former ones ensure the isotropy of material properties for example, the linear optical response of graphene does not dependent on the incident light polarization. Breaking C_3 or C_6 rotational symmetry by strain or structural confinement will enable in-plane anisotropy or even induce a pseudo magnetic field[30–32]. Time-reversal symmetry breaking by applying magnetic field or magnetic atom doping will lift the spin degeneracy and lead to more distinctive phenomena such as anomalous Hall effect and magneto-optical effects[33–36].

1.2 Organization of the dissertation

The remaining parts of the dissertation focus on engineering the symmetry breaking in both Van der Waals materials and photonic systems. Due to the analogy between Maxwell's and Schrodinger's equations, the concept of symmetry engineering and the resulting effects in different systems are comparable.

In Chapter 2, we demonstrate that by introducing a relative twist angle between bilayer graphene, the inversion symmetry of the bilayer structure breaks. We first probe the second harmonic generation (SHG) response of the twisted system to confirm the centrosymmetry breaking. Further polarization characterization reveals the SHG dependence on the point group of the system after twisting. Based on vectorial field theory, the magnitude of susceptibilities for samples with different twist angle is extracted. The relation between the dispersion of susceptibilities and the coupled energy bands are uncovered by theoretical simulation and twist angle dependent measurements.

In Chapter 3, we explore the possibility of inversion symmetry breaking by introducing birefringent material into two-dimensional photonic lattices via electromagnetic simulations. By using plane-wave expansion method, we show that the induced effective gauge field by 'tilted anisotropy' has the form of Rashba-Dresselhaus spin-orbit coupling (SOC) and spin-polarized bands split accordingly. The approach we adopted here is generic and can be applied to various photonic systems to successfully emulate and enhance SOC effects in their solid-state counterparts. By applying it to a photonic graphene ribbon structure, we show the emergence of spin-polarized edge states and spin-momentum locking over a limited range of wavenumbers. Furthermore, due to the degeneracy breaking of the spin-up and spin-down states, a photonic spin Hall effect is expected. By probing the field and phase distribution after the excitation of a spinless source, two counter-propagating spin-polarized bulk waves are demonstrated.

Chapter 2: Second Harmonic Generation (SHG) in twisted bilayer graphene (tBLG)

2.1 Motivations

The relative twist angle between two adjacent vdW layers has enabled a new degree of freedom in controlling of low dimensional van der Waals (vdW) materials' properties. Recent discoveries of superconductivity, correlated states and emergent ferromagnetism at the 'magic' twist angle revealed the strong interlayer coupling in twisted bilayer graphene (tBLG) systems[5,6,8,37,38]. Flattened bands with a high density of states, often denoted as van Hove singularities (vHs) or anti-crossings, are created in tBLGs when two Dirac cones from each individual layer intersect in momentum space[39]. Scanning tunneling spectroscopy (STS) has shown the twist-angle-dependent vHs by bringing it close to Fermi energy (E_F) through electronic gating[40]. Near these vHs, resonant optical effects, such as enhanced absorption, laser-wavelength dependent Raman, two-photon emission, and strong circular dichroism (CD), have been reported[41–45]. Recently, the excitonic nature of flattened bands in tBLG have also been demonstrated via the exploration of the dynamics of carrier relaxation under one-photon or two-photon resonant photoluminescence excitation (PLE) conditions and multiple transitions with different selection rules have been revealed[41].

The twisting degree of freedom not only allows strength tuning for interlayer coupling but also the overall symmetry of the system[38], which plays a critical role in various physical processes, including second harmonic generation (SHG). As is well-known, SHG is very sensitive to the symmetry of a material and has been widely accepted as a noninvasive tool for characterizing crystalline orientation and electronic structures[46]. Monolayers of many two-dimensional (2D) van der Waals materials such as hBN, MoS_2 and naturally stacked trilayer graphene have well defined D_{3h} symmetry without an inversion center, and SHG measurements from these materials have been reported[47,48]. There are also reports on the SHG from centrosymmetric monolayer graphene due to surface dipole and bulk quadrupole contributions, but these effects are usually weak[49]. SHG from symmetry-breaking bilayer graphene by applying in- or out-of-plane electric field have been theoretically proposed[13,50,51], but it is difficult to measure those processes experimentally due to their low working frequencies. For the observation of strong electric-dipole-enabled SHG, inversion symmetry breaking of the crystal structure and a larger scale of resonant energy are necessary[52].

In this part of the dissertation, we show a tunable SHG response in tBLGs with different twisting angles. The tunability is closely related to the change of intrinsic nonlinear dispersion of tBLGs. Moreover, due to the involvement of higher-order tensor in the nonlinear optical process, SHG measurement can unravel more underlying symmetry properties of the tBLG system compared to CD and other linear characterization means.

2.2 Prerequisite for second-order nonlinear effect

The response of semiconducting materials to the external optical field can be described as a collective oscillation of electric dipoles. When the external optical field is relatively weak, atoms in the solids are treated as harmonic oscillators and the Lorentz model captures the essential features[52]. In this linear region, the induced polarization can be written as: $\boldsymbol{P} = \varepsilon_0 \chi^{(1)} \boldsymbol{E}$, where $\chi^{(1)}$ is the conventional electric susceptibility of the material and is related to its relative permittivity by: $\chi^{(1)} = \varepsilon_r - 1$.

The harmonic approximation is only valid around the equilibrium position of the potential well. Under stronger external field, anharmonic terms are needed to be considered. Thus, a more general description of the optical response can be expressed as:

$$\boldsymbol{P} = \varepsilon_0 \chi^{(1)} \boldsymbol{E} + \varepsilon_0 \chi^{(2)} \boldsymbol{E^2} + \varepsilon_0 \chi^{(3)} \boldsymbol{E}^3 + \cdots$$

$\chi^{(2)}$ and $\chi^{(3)}$ are known as second- and third- order nonlinear optical susceptibilities and the terms associated with them are the nonlinear optical responses of the underlying material system.

Depending on the exact condition of input electric fields, the nonlinear optical phenomenon varies. Take the second order response as an example. If the input fields are monotonous:

$$\boldsymbol{E} = E e^{-i\omega t} + c.c.$$

The induced second-order polarization becomes:

$$\boldsymbol{P}^{(2)} = \varepsilon_0 \chi^{(2)} \boldsymbol{E^2} = 2\varepsilon_0 \chi^{(2)} + (\varepsilon_0 \chi^{(2)} E^2 e^{-2i\omega t} + c.c.)$$

The first term in the above expression is frequency independent which means its induced polarization will not change sign as the driving electromagnetic field. The process is referred to as optical rectification because it converts/rectifies an AC field to a DC one. The second term in the parenthesis has a 2ω frequency dependence. Consequently, the induced polarization $\boldsymbol{P}^{(2)}(2\omega)$ function as a new source at the doubled frequency and radiate which is called the second harmonic generation (SHG).

Consider the case when two electric field with different frequencies are involved in the second order process:

$$\boldsymbol{E} = E_1 e^{-i\omega_1 t} + E_2 e^{-i\omega_2 t} + c.c.$$

The nonlinear polarization now has more parts with different frequency dependences:

$$\boldsymbol{P}^{(2)} = \varepsilon_0 \chi^{(2)} \boldsymbol{E^2} = 4\varepsilon_0 \chi^{(2)} + \varepsilon_0 \chi^{(2)} \left(E_1^2 e^{-2i\omega_1 t} + E_2^2 e^{-2i\omega_2 t} + c.c.\right) + 2\varepsilon_0 \chi^{(2)} \left(E_1 E_2 e^{-i(\omega_1+\omega_2)t} + c.c.\right) + 2\varepsilon_0 \chi^{(2)} \left(E_1 E_2 e^{-i(\omega_1-\omega_2)t} + c.c.\right)$$

The four distinct terms correspond to optical rectification, SHG, sum frequency generation (SFG) and difference frequency generation (DFG) respectively.

As we have seen, multiple second-order phenomena are all associate with the same $\chi^{(2)}$. However, not all material systems possess finite value of $\chi^{(2)}$ and can be used for frequency conversion. Next, we will reveal how the spatial symmetry of the underlying solid crystal dictates the second-order susceptibility tensor.

The first symmetry element to be considered is the inversion. If we change the sign of incident field $\boldsymbol{E}$ and assume the crystal is inversion symmetric. The polarization relation is now given by:

$$-\boldsymbol{P}^{(2)} = \varepsilon_0 \chi^{(2)} (-\boldsymbol{E})^{\boldsymbol{2}}$$

which can also be shown as: $\boldsymbol{P}^{(2)} = -\varepsilon_0 \chi^{(2)} \boldsymbol{E}^{\boldsymbol{2}}$. Compared to the previous definition, the only possible solution is that $\chi^{(2)} = 0$. Therefore, inversion symmetry breaking is the prerequisite for observing second order effects. Besides, due to the vector nature of electric fields and polarization, $\chi^{(2)}$ is a third-order tensor ${\chi_{ijk}}^{(2)}$. Nonzero elements in the tensor can further be reduced by considering the symmetry class of the crystal.

2.3 Inversion symmetry breaking enabled by twisting

Intuitively, stacking two layers of centrosymmetric materials would not give rise to strong SHG with only surface interactions. Due to the breaking inversion symmetry and strong interlayer couplings resulting from the twist in tBLG systems, SHG comes from the entire two-layer material instead of the interface. As shown schematically in Figure 2.1, naturally stacked bilayer graphene remains centrosymmetric whether they are any kinds of translational displacement (T). This is not true, however, if a relative twist angle other than 0° or multiples of 60° is introduced by a rotational operation (R).

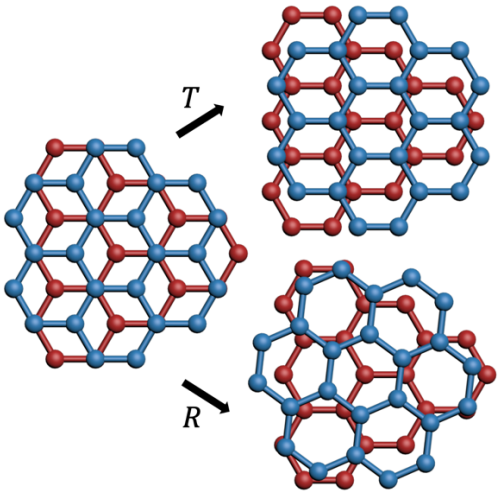

Figure 2.1 Schematics of bilayer graphene and tBLG. AB-stacked bilayer graphene crystal structure with an additional translational replacement (T) and relative twist (R). The top and bottom layers are labeled as blue and red, respectively.

It can be mathematically proven that: if we invert the top graphene layer through an arbitrary point in the middle plane, it cannot overlap with the bottom layer. As shown in Figure 2.2, for any two lattice point in top layer (red): (x_1, y_1, z_1), (x_2, y_2, z_1) and an arbitrary point in the middle plane: (x_0, y_0, z_0), the inverted corresponding points would be: $(2x_0 - x_1, 2y_0 - y_1, z_2)$, $(2x_0 - x_2, 2y_0 - y_2, z_2)$. It is obvious that the difference between red graphene layer and the inverted yellow one is purely translational. In another word, with a predefined twist between blue and red

graphene layer, there is no way that the red layer can overlap with the blue layer only with inversion operation. Therefore, there is no inversion-symmetry in tBLG system.

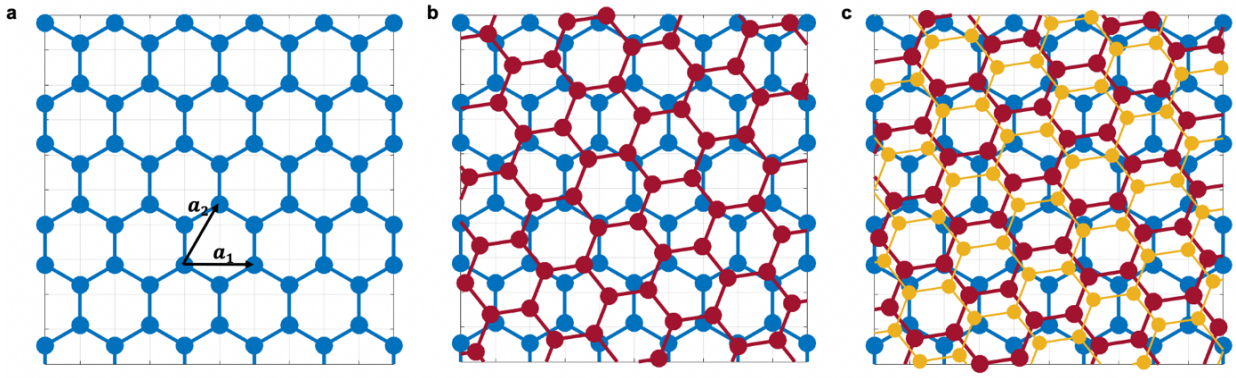

Figure 2.2 (a) A single layer graphene. (b) Staking another layer graphene (red) on top of the one in a (blue) with an extra twist (not equal to 0° or multiples of 60°). (c) The inverted version of top layer graphene (yellow) is achieved by inverting red layer with respect to an arbitrary point in the middle plane.

Therefore, the bilayer structure lacks the inversion symmetry which is the case for tBLGs. The above proof and the strong interlayer coupling in tBLG systems which is manifested as vHs in the density of electronic states of the system, allows SHG to be generated from the entire two-layer material instead of the interface.

In addition, the transition between vHs points in the valance and conduction bands (E_{vHs}) can further contribute to SHG enhancement when incident photons fulfill 1- or 2- photon resonant SHG conditions, giving rise to a twist-angle dependent SHG response. Therefore, the mechanism for SHG demonstrated is enabled by the hybridized electronic states engineered by the twisting degree of freedom and the mechanism is different form the twisted transition metal dichalcogenide (TMDC) systems. Since TMDC itself is non-centrosymmetric, varied SHG emissions from layered TMDC are due to SHG interference between single layers. On the other hand, in tBLG, constituting graphene is centrosymmetric and the SHG comes from inversion symmetry breaking in the hybrid graphene layers. More specifically, in layered TMDC, SHG efficiency changes with twist angle due to different interference conditions[27,53] (constructive, destructive or partially constructive) instead of different degree of hybridization between layers. In tBLG, however, the twist completely changes the symmetry of the materials, and the efficiency is determined by the underlying hybrid electronic structure. Therefore, it is more sensitive to the twisting compared to TMDC and shows pronounced enhancement when the incident energy matches E_{vHs}.

2.4 Synthesis and characterization of tBLG with different twisting angles

TBLG samples were prepared by a dry transfer method, with which different twisting angles can be realized. Before picking up the upmost hBN layer using polypropylene carbonate (PPC) stamp, we conducted SHG mapping on the exfoliated hBN nanosheets to ensure that they are uniform and even-layered, which excludes possible contributions from hBN in the final SHG results. By attaching the stamp on a vertical stage and the substrate on a rotatable mount, we are able to pick up hBN and use this hBN to pick up one half of the graphene layer. By rotating the mount with another half of graphene layer on it to the desired angle and align it with the previous half on the stamp, a tBLG sample can be made.

To further avoid strain-induced effects at the interface from bubbles between hBN and the first layer of graphene, we adopted the recently published method[54] by stacking hBN onto graphene at a high temperature. which resulted in a relatively clean surface in the twisted region like the one shown in Figure 2.4a. It can also be readily identified under the optical microscope (highlighted with the red box).

The angles of the sample were verified by Raman measurements under 532nm excitation (Figure 2.3b). Comparison of Raman spectra of the tBLG and single-layer graphene for the sample in Figure 2.4a is plotted in Figure 2.3a. The peak around 1366 cm^{-1} is attributed to hBN. The R peak showing up on higher wavenumber side of the G peak at 1627 cm^{-1} is usually associated with the intervalley double-resonance process in tBLG systems[42] and corresponds to the twist angle around 8° in this case.

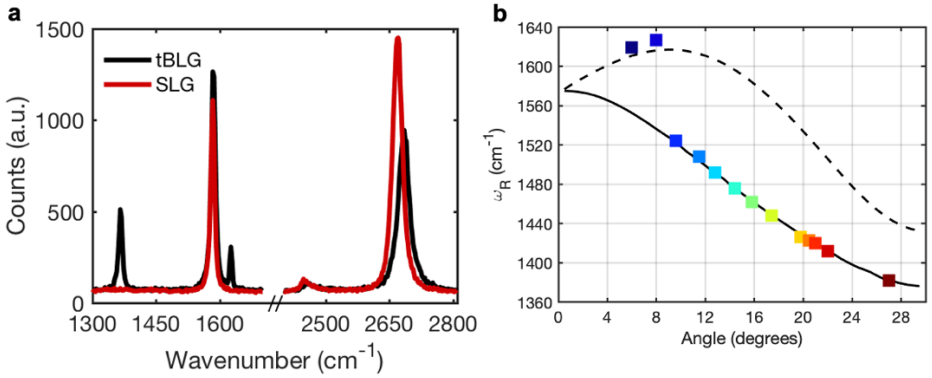

Figure 2.3 (a) Raman spectra of a 8° tBLG sample under hBN (black) and monolayer graphene (red) under 532nm excitation. (b) Raman R peak frequencies from tBLG samples with different twist angles under 532nm incident laser. The R peak form 0° and 4° samples didn't show up during measurement due to the fact that the double-resonance energy of these samples are much smaller than the incident laser energy. The R peak positions are achieved by Lorentzian fitting of Raman spectrum.

Figure 2.4b shows the integrated intensity of the Raman R peak across the whole sample. The sharp contrast between the twisted and untwisted regions is clear, matching those in the optical image. Figure 2.4c shows the SHG mapping of the same area by exciting the sample with a continuous wave (CW) laser at the wavelength of 1064nm under normal incidence with collection

signal around 532nm. From the mapping results, we can clearly identify a strong emission in the tBLG region and its second-order nature is confirmed by the power-dependent measurement plotted in Figure 2.5a. SHG spectra of tBLG with 6° twist angle, trilayer graphene (TLG), and CVD grown monolayer MoS_2 are shown in Figure 2.5b. The inset compares the SHG efficiency of these three materials under the same conditions and SHG from tBLG is comparable to monolayer MoS_2 at this wavelength. Based on the vector model[55], we calibrated the nonlinear susceptibility of 6° twist angle to be around $28 \times 10^4\ pm^2/V$ under resonant excitation condition, which is comparable to the on-resonant susceptibility of monolayer MoS_2[47,56,57].

Another notable feature is that the SHG spectrum of tBLG has only one sharp peak centered around 532nm without any broadband nonlinear photoluminescence, which is contrary to the case when the excitation and relaxation processes are on the femtosecond scale[58–60]. Although there are theoretical predictions on the emergence of SHG in graphene/hBN system due to sublattice asymmetry in the graphene layer[13], it cannot account for the results we observed here. For those regions which consist of monolayer graphene and hBN, there are no detectable SHG signals. The fact that we did not observe any SHG signal from pure graphene layer on SiO_2/Si substrate (highlighted with the blue box in Figure 2.4a) also rules out the possibility that the observed SHG signal arises from the breaking of inversion symmetry of graphene by the presence of the oxidized silicon substrate[49].

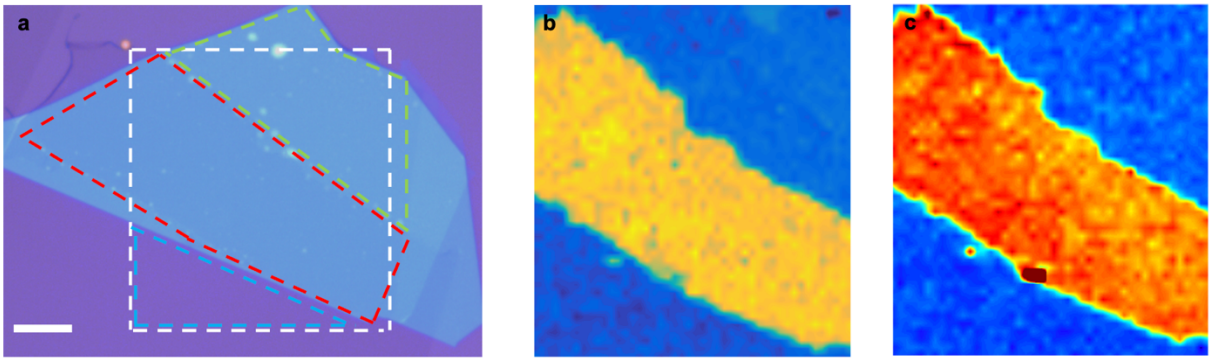

Figure 2.4 (a) Optical image of a tBLG with 8° twisted angle. The tBLG region, single-layer graphene region under hBN and pure single-layer graphene on substrate region are indicated by red, green and blue dashed boxes. The white box corresponds to the following mapping area. (b and c) Raman R peak mapping and SHG mapping of the 8° tBLG sample using 532nm and 1064nm CW laser respectively. Scale bar: 10um.

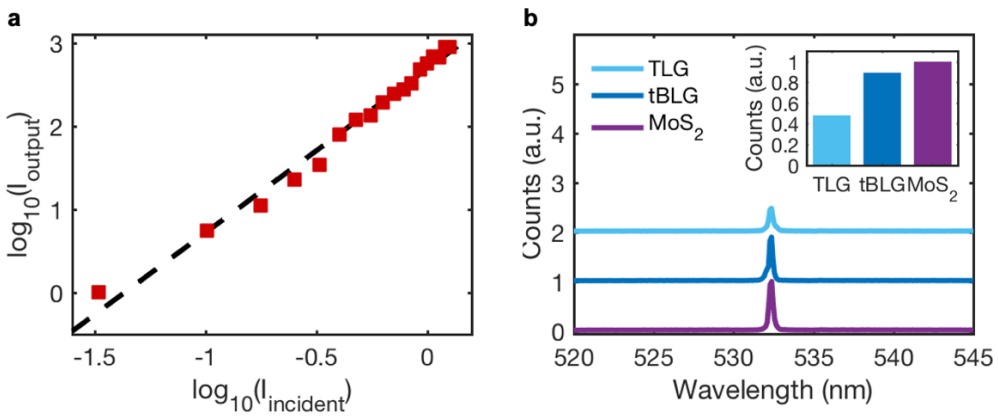

Figure 2.5 (a) SHG power dependence of 8° tBLG sample in log-log scale. The dotted data (red) were fitted linearly with a slope of 1.97±0.06 (a.u.). (b) SHG spectra of TLG (light blue), tBLG (dark blue) and CVD-grown monolayer MoS_2 (purple). The spectra are shifted vertically for a clearer view. The insert compares the relative amplitude of the SHG signal of three species under the same experimental configuration excited by 1064nm CW laser.

2.5 Polarization dependence

SHG mapping and polarization measurement setup is shown in Figure 2.6. Excitation beam from a CW laser is first sent through a linear polarizer (LP) orientated in X direction and then focused on to the sample by a high-NA objective lens. TBLG samples are mounted on an XY Piezo Stage to achieve spatial SHG resolution. Emission from the sample is first collimated by the objective lens, then filtered by a short pass filter (SP) to get rid of excitation beam. Finally, the SHG emission is focused onto the silt of the spectrometer with silicon detector by a detector lens (L). For polarization measurement, another polarizer is placed perpendicular to the excitation polarization (Y direction) before the detector lens and the sample is rotated around the sample normal. The setup for Raman measurement is similar to the SHG except that the laser has a wavelength at 532nm (CW), and the SP is replaced by a 532nm Raman filter.

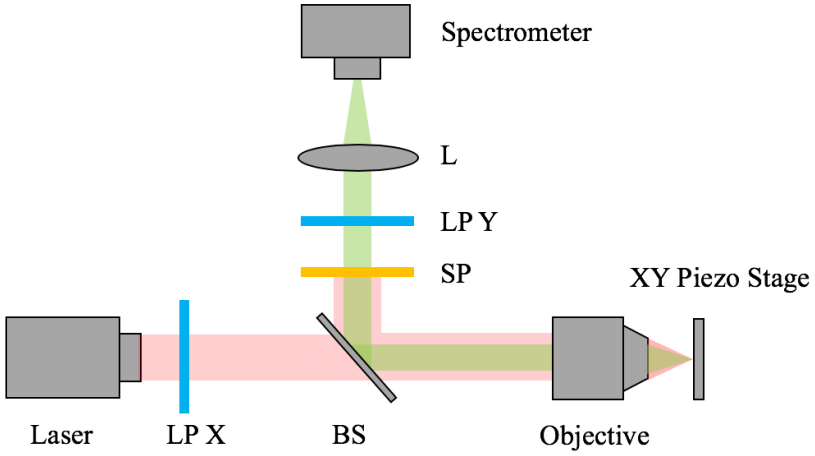

Figure 2.6 Schematic of experimental setup for SHG mapping and polarization measurement. LP X and LP Y are two linear polarizers polarized in X and Y direction respectively. SP is a short pass filter and L is a detector lens.

One of the CW laser models we used in this work was a Ventus 1064 (Laser Quantum) and the maximum power output was 100mW. The power after the objective lens was measured to be 90 mW, and the focused light spot was ~4.5 um. The second CW laser system we used was a Littman/Metcalf 785 nm (Sacher Laser technik) with output power 100 mW, and the focused light spot was ~4 um.

As such, the SHG signal is very sensitive to the underlying symmetry of the material, and we explored the contributions from different components using the SHG polarization method. Although the inversion symmetry is broken in tBLG samples, the exact point-group symmetry cannot be accurately defined because of different choices of the twisting center. For example, at a specific commensurate twist angle, the point-group symmetry of tBLG is either D_3 or D_6 depending on whether the twisting center is carbon atom or hexagonal center. In addition, the symmetry will reduce to C_3 or C_6 if the angles become incommensurate[38,61]. However, it has been reported that the exact symmetry of tBLG may only affect the electronic behavior of the system on the scale of meV. The susceptibility calculations shown below also suggests that it is the universal chirality instead of the exact symmetry of tBLG system that determines the ultimate SHG response.

Closer investigation on the second-order susceptibility of tBLG with different point-symmetry shows that it is always possible to find a non-zero tensor component χ_{xyz} associated with the chirality[62,63]. Moreover, the resonant and dispersive behavior of tBLG in the visible range due to the semimetal and anticrossed band structure point towards the failure of Kleinman symmetry in describing the second-order susceptibility[64]. Thus, the contribution from the chiral tensor component χ_{xyz} cannot be neglected here and this prediction agrees with both DFT simulations[65] and our SHG polarization measurements as shown below.

We use linearly polarized excitation at λ=1064nm with normal incidence through an objective lens with a numerical aperture NA=0.9. We rotated the sample with respect to the laser axis and collected reflected SHG signal using the cross-polarization configuration. The six-fold symmetric pattern from an odd-layer of hBN (Figure 2.7a) is representative of a D_{3h} system, and the signal is determined by only one independent tensor component: $I_v \propto \left|\chi_{yyy} \sin(3\theta)\right|^2$, which is consistent with previous reports[47]. However, tBLG samples do not yield same results under the same experimental configuration. As shown in Figure 2.7b, 2.7c, and 2.7d with 8°, 10°, and 12° twist angles respectively, the twist angles are determined by the frequency of Raman R peak before SHG measurements. A clear threefold symmetry can be identified in all tBLG samples.

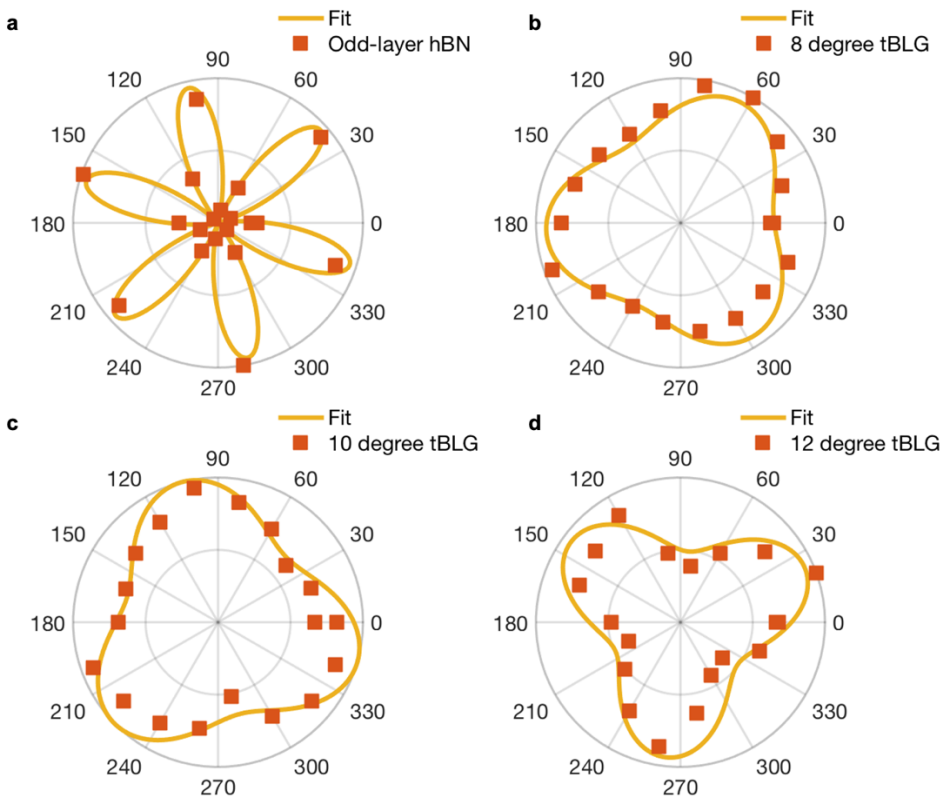

Figure 2.7 (a-d) SHG polarization pattern of an odd-layer hBN, 8°, 10°, and 12° tBLG samples respectively with a polarizer vertical to the polarization of incident laser before the detector.

From DFT calculations of a commensurate tBLG model with different twisting centers, we find that the SHG process is dominated by a nearly constant χ_{xyz} independent of the centers. In Figure 2.8a and 2.8b, we plot all in-plane tensor components of a 21.8° tBLG with the carbon atom being the twisting center. The 21.8° commensurate angle is chosen because of the computational efficiency and the space group is C_3 for this specific translational configuration[42,43]. Thus, due to symmetry reasons, the spectral response of $|\chi_{xyz}|$ ($|\chi_{xyy}|$) is the same as $|\chi_{yxz}|$ ($|\chi_{yxy}|$) with other in-plane tensor elements being negligible.

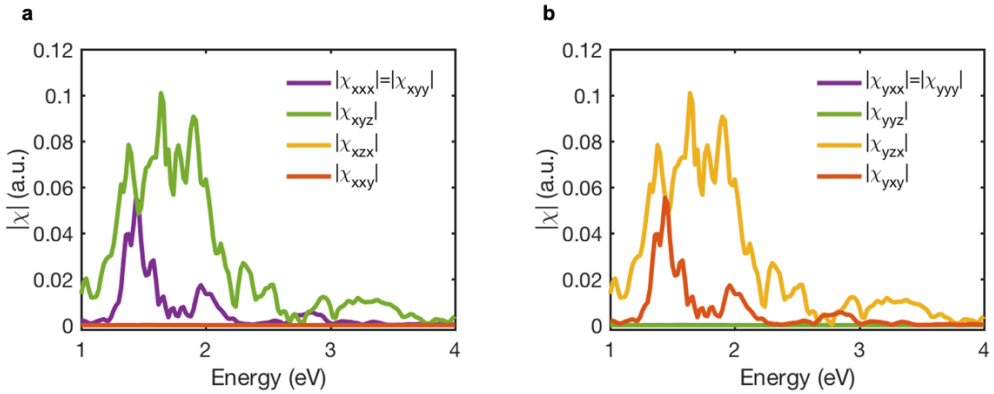

Figure 2.8 (a-b) DFT calculation of second-order susceptibility response in x and y direction of a 21.8° tBLG model.

More spectral responses of second-order tensors with different twisting centers are shown in Figure 2.9, Figure 2.10 and Figure 2.11. It can be seen that non-chiral tensors also contribute and evolve with the interlayer shift except for the AA-like stacking case. However, they show a weak dependence on the twisting center overall[61]. Therefore, we can fit the polarization results with the dominant χ_{xyz} component and the next non-vanishing one, χ_{xxx}. Fitting curves are also shown in Figure 2.7, which agrees well with the experimental results. The detail of the fitting will be elaborated in the next part.

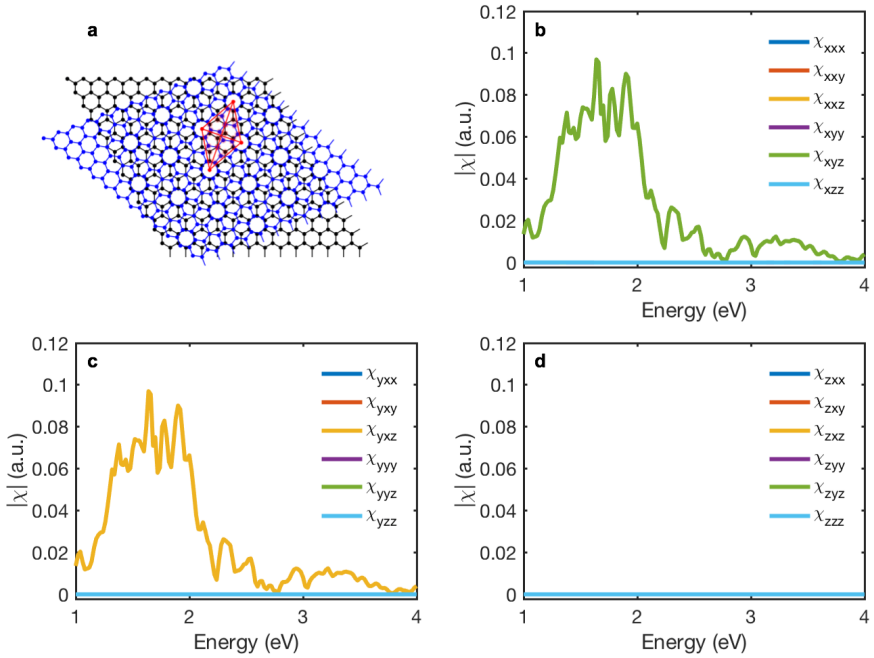

Figure 2.9 (a) Schematic of the AA stacked tBLG with 21.8° twist. The symmetry is D_6. The red box outlines the unit cell. (b-d) Spectral response of the susceptibility tensors along x, y, and z-direction.

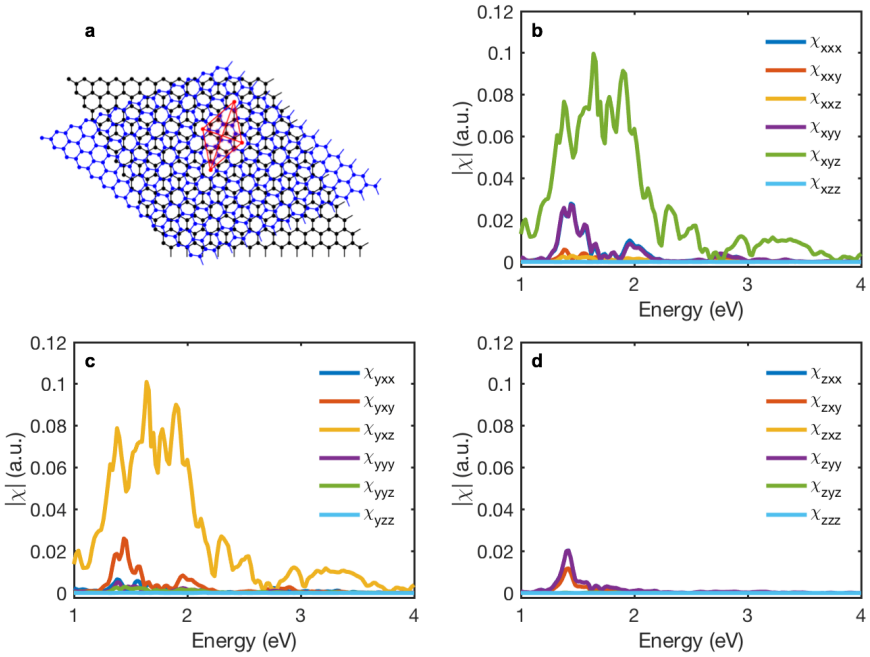

Figure 2.10 (a) Schematic of a 21.8° tBLG with an additional translation displacement ($1/3\vec{a}$) along the lattice vector ($\vec{a}$) as respect to AA stacked configurationThe symmetry is C_1. (b-d) Spectral response of the susceptibility tensors along x, y, and z-direction.

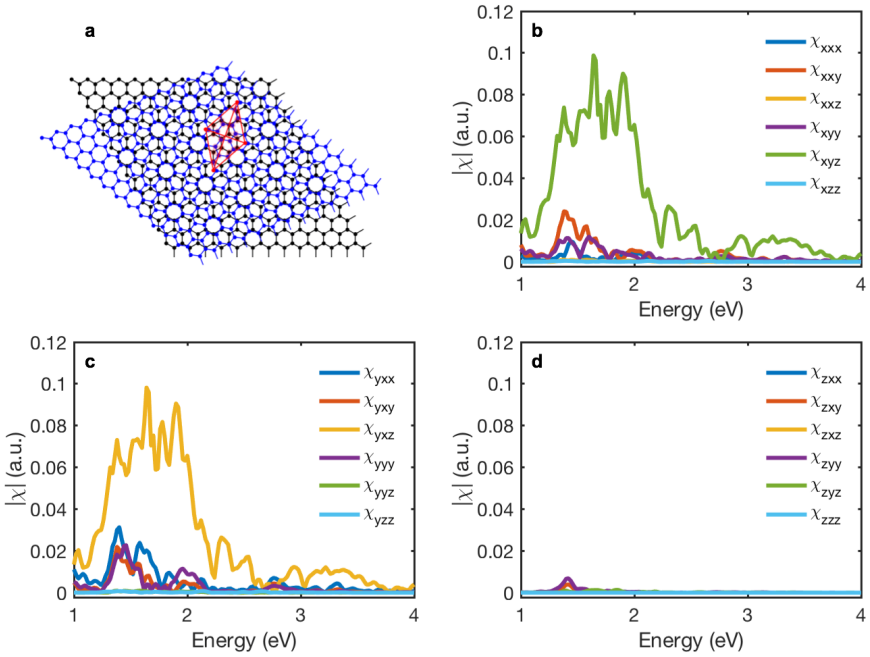

Figure 2.11 (a) Schematic of a 21.8° tBLG with an additional translation displacement ($2/3\vec{a}$) along the lattice vector ($\vec{a}$) as respect to AA stacked configuration. The symmetry is C_1. (b-d) Spectral response of the susceptibility tensors along x, y, and z-direction.

Owing to the high NA of the objective lens used, there will always be a finite portion of z polarized light illuminated on the sample and be converted to in-plane polarized SHG field via the χ_{xyz} component[66–68]. By reducing the NA, the proportion of z-polarized field is also diminished resulting in a more drastic decrease of SHG efficiency of tBLGs compared to MoS_2. The comparisons are shown in Table 2.1. When we change the NA from 0.9 to 0.75 or 0.5, due to reduced collection efficiency, SHG from both material decrease dramatically. However, it is still clear that the SHG intensity drop of tBLG is more obvious than MoS_2 under the same experimental condition. Thus, we attribute part of the SHG signal of tBLG collected using 0.9 NA objective lens to the z-polarized incident field and include this factor in the polarization fitting part.

NA ratio	6° tBLG	MoS2
0.75NA/0.9NA	0.254	0.379
0.5NA/0.9NA	0.097	0.229

Table 2.1 SHG intensity ratio of 6° tBLG and monolayer MoS_2 using different NA objective lens.

2.6 Nonlinear susceptibility calibration

The most general relation between second-order polarization and incident electric field can be written as:

$$\begin{bmatrix} P_x(2\omega) \\ P_y(2\omega) \\ P_z(2\omega) \end{bmatrix} = \epsilon_0 \begin{bmatrix} \chi_{xxx} & \chi_{xyy} & \chi_{xzz} & \chi_{xyz} & \chi_{xzx} & \chi_{xxy} \\ \chi_{yxx} & \chi_{yyy} & \chi_{yzz} & \chi_{yyz} & \chi_{yzx} & \chi_{yzz} \\ \chi_{zxx} & \chi_{zyy} & \chi_{zzz} & \chi_{zyz} & \chi_{zzx} & \chi_{zzz} \end{bmatrix} \begin{bmatrix} E_x^2(\omega) \\ E_y^2(\omega) \\ E_z^2(\omega) \\ 2E_y(\omega)E_z(\omega) \\ 2E_x(\omega)E_z(\omega) \\ 2E_x(\omega)E_y(\omega) \end{bmatrix}$$

For monolayer MoS_2 with D_{3h} symmetry, the SH susceptibility reduces to the following form with only one independent tensor component:

$$\begin{bmatrix} \chi_{xxx} & -\chi_{xxx} & 0 & 0 & 0 & 0 \\ 0 & 0 & 0 & 0 & 0 & -\chi_{xxx} \\ 0 & 0 & 0 & 0 & 0 & 0 \end{bmatrix}$$

Therefore, for MoS_2 the detected SH signal without any polarizer before the detector (LP Y) is:

$$I_{MoS_2}(2\omega) = C\chi_{xxx}^2 I(\omega)^2,$$

where C is a proportionality constant determined by the local dielectric environment[56] and $I(\omega)$ is the intensity of incident fundamental field. For tBLG we can reduce the tensor matrix according to C_3 crystal symmetry and there are 8 independent elements left:

$$\begin{bmatrix} \chi_{xxx} & -\chi_{xxx} & 0 & \chi_{xyz} & \chi_{xzx} & -\chi_{yyy} \\ -\chi_{yyy} & \chi_{yyy} & 0 & \chi_{yyz} & -\chi_{xyz} & -\chi_{xxx} \\ \chi_{zxx} & \chi_{zxx} & \chi_{zzz} & 0 & 0 & 0 \end{bmatrix}$$

Based on our SHG DFT simulation results only χ_{xyz} and χ_{xxx} are nonzero for C_3 symmetry. Assuming the same incident and local environment condition as MoS_2, which is valid in our experiment, the SHG from tBLG is:

$$I_{tBLG}(2\omega) = C(\chi_{xxx}^2 + 4f^2\chi_{xyz}^2 - 4f\chi_{xxx}\chi_{xyz}\sin(3\theta))\, I(\omega)^2,$$

The DFT results of tBLGs show that χ_{xxx} is much smaller than χ_{xyz}. Thus, we can use $I_{tBLG}(2\omega) = C(4f^2\chi_{xyz}^2)I(\omega)^2$ to get a lower bound for the estimation of tBLG susceptibility. Here f is the ratio of how much z-polarized light is converted by the high NA objective lens.

Due to the vectorial nature of light-matter interaction in the second order, the field distribution in the focal volume of a high-NA objective cannot be described by paraxial approximation anymore and the longitudinal component of polarization are nonnegligible[66,67]. Therefore, we adopt the vectorial Debye diffraction theory here to analyze the field distribution of fundamental light at focal plane and estimate the value of f in the above expression.

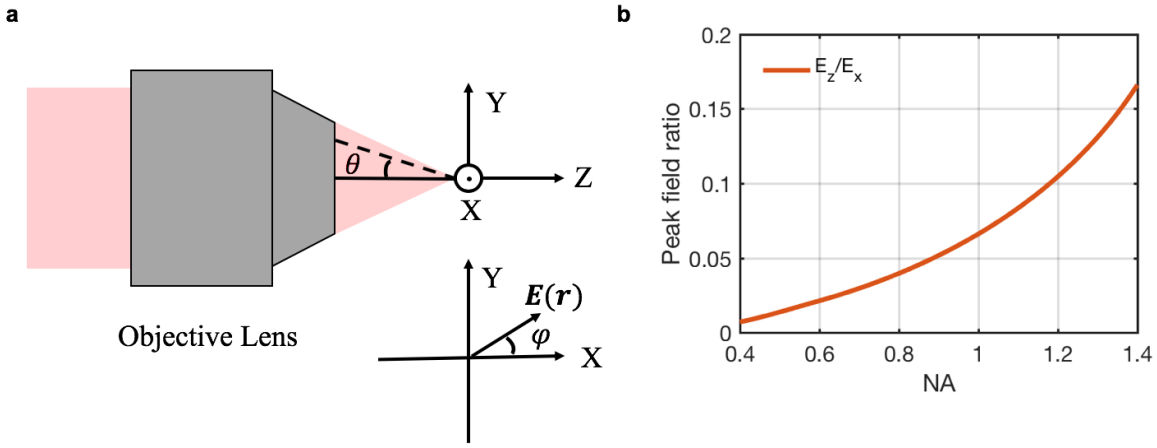

Figure 2.12 (a) Cross sectional view of the illuminating setup. The optical axis is along Z direction and samples lie on XY plane. $E(r)$ demotes the in-plane component of the fundamental field. (b) Peak field ratio E_z/E_x of fundamental field on the focal plane versus different NA value.

As schematically shown Figure 2.12a, the illuminating part of SHG measurement consists of a high NA objective lens and we will only consider linearly polarized fundamental field (X polarized) for further discussion. Based on the integral formula from Richard and Wolf[55], when incident light is polarized in X direction by an infinity-corrected objective, the electric field at focal plane can be expressed as:

$$E_x(\boldsymbol{r}) = -i[I_0 + I_2\cos(2\varphi)]$$
$$E_y(\boldsymbol{r}) = -iI_2\sin(2\varphi)$$
$$E_z(\boldsymbol{r}) = -I_1\cos(\varphi)$$

And the integrals I_n are defined as:

$$I_0 = \int_0^\alpha \cos(\theta)^{1/2}\sin(\theta)(1+\cos(\theta))J_0(krsin(\theta))\exp(ikzcos(\theta))d\theta$$
$$I_1 = \int_0^\alpha \cos(\theta)^{1/2}\sin(\theta)^2 J_1(krsin(\theta))\exp(ikzcos(\theta))d\theta$$

$$I_2 = \int_0^{\alpha} \cos(\theta)^{1/2} \sin(\theta)(1-\cos(\theta)) J_2(krsin(\theta)) \exp(ikzcos(\theta)) d\theta$$

Where φ is the azimuthal and of point **r** in the focal plane, θ characterizes the incident angle which spans form 0 to α, the maximal angle determined by the NA of illumination objective ($\alpha = \sin(NA/n)^{-1}$).

Figure 2.12b shows the peak intensity and field ratio of the longitudinal Z component versus transverse X component at the focal plane as a function of NA for 1064nm incident light. The Y-polarized component is neglected due to its extremely small value. For the specific objective lens we used (NA=0.9), E_z/E_x, i.e., f value, is about 0.1 ~ 0.2 which is consistent with previous calculations[35]. Moreover, the ability to efficiently collect the emission from dark excitons in TMDC using high NA objective (NA=0.82) has been experimentally achieved[68], where the authors estimates the percentage of z-polarized component to be around 9%, and agrees with our result.

By adding analyzer vertical or parallel to the incident laser polarization and rotate the sample around the laser axis, we can find that the SHG polarization pattern of tBLG satisfies following expression, respectively:

$$I_{vertical}(\theta) \propto (2f\chi_{xyz} + \chi_{xxx}\sin(3\theta))^2$$
$$I_{parallel}(\theta) \propto \chi_{xxx}^2 \cos(\theta)^2 (1 - 2\sin(2\theta))^2$$

Here, we take f to be 0.1 following above analysis and fit the experimental vertical polarization results with $I_{vertical}(\theta)$. We find that only when χ_{xyz} is much larger than χ_{xxx}, a good fit can be attained. Since χ_{xxx} is a small value, $I_{parallel}$ becomes almost two orders of magnitude smaller than $I_{vertical}$ and the SHG signal with a parallel analyzer falls below the detection limit of our system during measurement. Therefore, we are not able to fit parallel polarization results and obtain more quantitative estimations of the value of χ_{xyz} and χ_{xxx}. Figure 2.13 shows polarization result with two kinds of the analyzer for an odd-layer hBN and a tBLG sample.

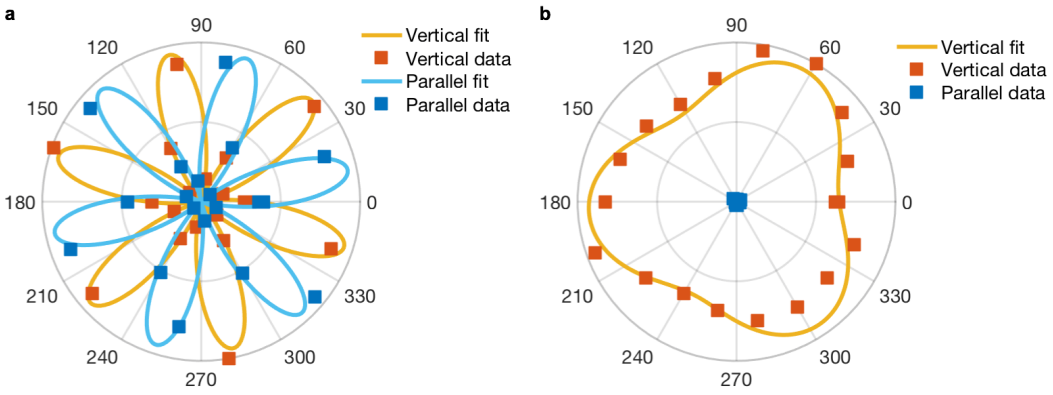

Figure 2.13 (a) SHG polarization results of an odd-layer hBN with vertical and parallel analyzer respectively. (b) Polarization results of 8° tBLG sample. SHG signal of tBLG with a parallel analyzer falls below the detection limit of our system.

To further reveal the field distribution of X-polarized incident field focused by a high NA objective (NA=0.9), we plot the magnitude and phase of E_x and E_z at focal plane in Figure 2.14 based on the same integral formula. As we can see in Figure 2.14a and 2.14c, E_x is rotationally symmetrical and is in phase in the region of interest while the magnitude peaks of E_z locate at the X axis and are out of phase (Figure 2.14b and 2.14d). It is the overlap between E_x and E_z field that is responsible for the SH response through χ_{xyz}.

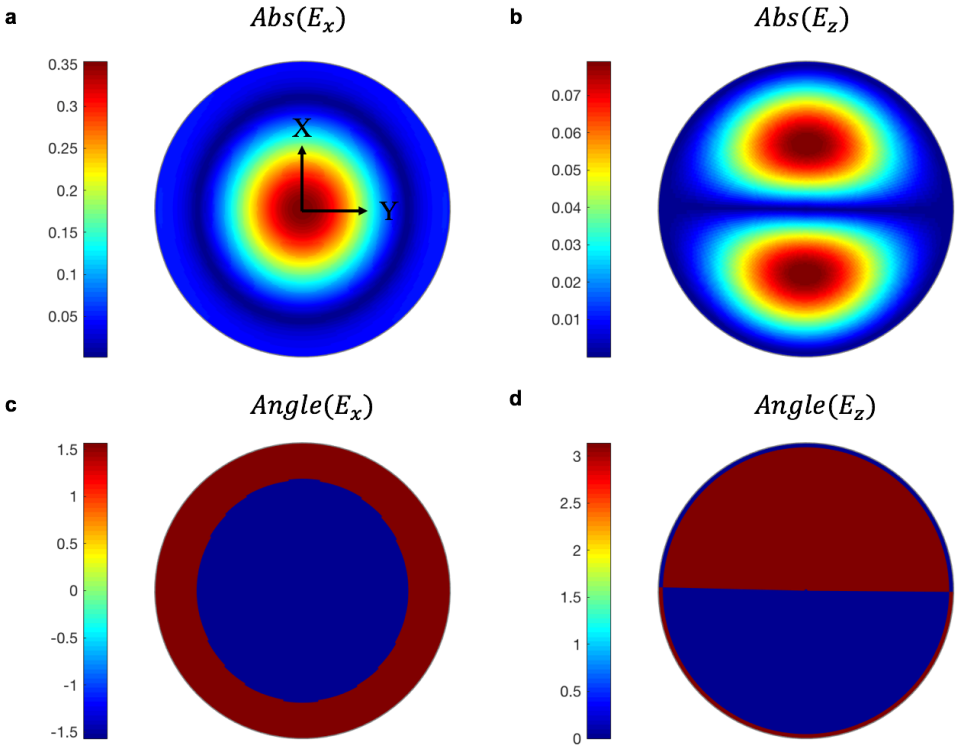

Figure 2.14 (a) The magnitude distribution of E_x and E_z at the focal plane by an objective lens with NA=0.9. In-plane coordinates are indicated. (b) The magnitude distribution of E_z. (c) The phase distribution of E_x at the same plane. (d) The phase distribution of E_z.

Although one might think that the SHG contributed from out-of-phase E_z field will cancel each other in the far field intuitively, we will show that this is not the case by taking into account the phase factor in vectorial Debye theory when simulating the SHG collection process in the followings.

Since the SHG process of MoS_2 has been well studied and calibrated[47,55,56], it serves as an excellent reference to calibrate the nonlinear susceptibility of the tBLG. Having the estimation of *f*, we can calculate the susceptibility of tBLG and trilayer graphene based on measured data. Consider trilayer graphene (TLG), 6° tBLG, and monolayer MoS_2 SHG measurements under the same conditions (same 1064nm CW laser, excitation power, optical setup, laser focus, substrate). Since TLG has the same symmetry as MoS_2, the equation governs SHG efficiency would also be the same with only one independent tensor for both systems. Therefore $\frac{\chi_{xxx,TLG}}{\chi_{xxx,MoS_2}} = \sqrt{\frac{I(2\omega)_{TLG}}{I(2\omega)_{MoS_2}}}$.

Following the above analysis for tBLG, we get $\frac{\chi_{xyz,tBLG}}{\chi_{xxx,MoS_2}} = \frac{1}{2f}\sqrt{\frac{I(2\omega)_{tBLG}}{I(2\omega)_{MoS_2}}}$. Taking the SH susceptibility of MoS_2 around 1064nm from theoretical and experimental work which is ~0.7 (10^4 pm^2/V), we get $\chi_{xxx,TLG}$ is about 0.49 (10^4 pm^2/V) and $\chi_{xyz,tBLG}$ is approximately 1.7 ~ 3.3 (10^4 pm^2/V). It can be seen that the susceptibility of on-resonance tBLG is higher than off-resonant MoS_2, but generally on the same order of 10^4 pm^2/V. The results from DFT calculation shown in Figure 2.8f-2.8e for 21.8° commensurate angle tBLG further confirm our evaluation. At resonance, χ_{xyz} is indeed on the same order of the result from experimental data.

The above evaluation of nonlinear susceptibility for tBLG is overly underestimated due to the ignorance of χ_{xxx} and the fact that E_z field only has finite overlap with E_x in the focal region. In order to get a more accurate estimation of χ_{xyz} for the 6° tBLG under resonant excitation, we simulate the evolution of SH signal through the detecting system with spatially varying E_x and E_z in the framework of vectorial Debye diffraction model. The detecting system of SH signal is shown in Figure 2.15 with the same objective lens as in the illuminating system (Figure 2.12a).

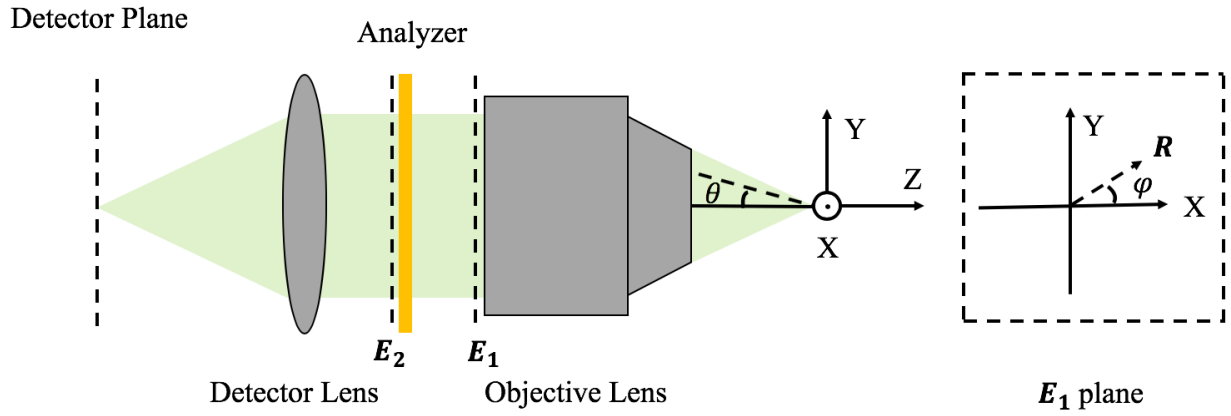

Figure 2.15 Schematic of the SHG collecting system. Emitted SHG signal is first collected by an objective with NA=0.9, then passes through an analyzer polarized in Y direction and finally focused onto the slit of spectrometer by a detector lens. *R* denotes the SH field points in E_1 plane.

In the simulation, the induced second-order polarization in tBLG sample can be taken as a two-dimensional collection of dipoles, of which the directions are determined by the nonlinear tensors. The far-field radiation can be calculated as the superposition of all these dipoles:

$$E_{dipoles} = \frac{e^{2ikR}}{4\pi R}\int e^{-2iks\cdot r}\{\boldsymbol{s}\times[\boldsymbol{s}\times\boldsymbol{P}(\boldsymbol{r})]\}dr^2$$

Where $\boldsymbol{P}(\boldsymbol{r})$ is the induced SH polarization, $E_{dipoles}$ is the radiated SH field, R is the observation point at plane $\boldsymbol{E_1}$ behind the objective, r is the coordinate in the focal plane and s is the unit vector in the observation direction.

Following the standard method[55], the electric vectors ($\boldsymbol{E_1}$) of SH signal behind the collimating objective is:

$$E_{1x} = \cos(\theta)^{-\frac{1}{2}}(-a_1 B_x - a_2 B_y + a_3 B_z)$$
$$E_{1y} = \cos(\theta)^{-\frac{1}{2}}(-a_2 B_x - a_4 B_y + a_5 B_z)$$
$$E_{1z} = 0$$

Where

$a_1 = \sin(\varphi)^2 + \emptyset \cos(\varphi)^2 \cos(\theta)$

$a_2 = \sin(\varphi)\cos(\varphi)(\cos(\theta) - 1)$

$a_3 = \cos(\varphi)\sin(\theta)$

$a_4 = \sin(\varphi)^2 \cos(\theta) + \cos(\varphi)^2$

$a_5 = \sin(\varphi)\sin(\theta)$

$$B_x = \frac{e^{2ik_2R}}{4\pi R}\int e^{-2ik_2 s\cdot r} P_x dr^2$$

$$B_y = \frac{e^{2ik_2R}}{4\pi R}\int e^{-2ik_2 s\cdot r} P_y dr^2$$

$$B_z = \frac{e^{2ik_2R}}{4\pi R}\int e^{-2ik_2 s\cdot r} P_z dr^2$$

Here, θ and φ are polar and azimuthal angles of the observation point R as shown in Figure 2.15, k_2 in the integral is now the wavevector of SH field at doubled frequency of the fundamental wave. In the paraxial approximation, we usually assume emitted SH field vectors to be linearly proportional to the induced SH polarization vectors. However, as we can see in the above expressions, cross-effect between lateral and longitudinal components are possible in the presence of a high-NA objective. In our case, the induced Z-polarized second-order polarization ($\chi_{z\cdot\cdot}$) is negligible according to the DFT results, and we only need to consider the collection of induced P_x and P_y.

Behind the objective, another Y-orientated linear polarizer (perpendicular to the incident polarization) is placed before the detecting lens to select cross-polarized SH field. The final detector lens with low NA is used for focusing SH signal to the detector. The collected SH power, therefore, can be calculated by integrating SH field intensity over a spherical surface of radius R within the cone angle of the collimating objective:

$$I = \int_0^{\alpha} d\theta \int_0^{2\pi} d\varphi |\boldsymbol{E}_2(\boldsymbol{R})|^2 \boldsymbol{R}^2 \sin(\theta)$$

For SHG intensity simulations of MoS_2 and tBLG, we apply the same incident field, which is the same field distribution enabled by an objective with 0.9 NA as calculated in Figure 2.14. We keep the incident light to be polarized in X direction and rotate the sample around the normal direction. The angle between X direction in lab frame and x direction in local fame of sample is β.

For MoS_2, the induced polarization expressed in global coordinates can be expressed as:

$$E_x = E_X \cos(\beta) + E_Y \sin(\beta)$$
$$E_y = -E_X \sin(\beta) + E_Y \cos(\beta)$$
$$P_x = \chi_{xxx} E_x^2 - \chi_{xxx} E_y^2$$
$$P_y = -2\chi_{xxx} E_x E_y$$

$$P_X = P_x \cos(\beta) - P_y \sin(\beta)$$
$$P_Y = P_x \sin(\beta) + P_y \cos(\beta)$$

We take the off-resonant susceptibility value of MoS_2 to be 0.7 (10^4 pm^2/V) as reported. Results shown in Figure 2.16 are SHG polarization results of MoS_2 with a Y-orientated analyzer before the detector from the spatial distribution of incident field using the Vector model (orange dots) and from a simple analytical model ($I(\omega) = C\chi_{xxx}^2 \cos(3\beta)^2 I(\omega)^2$) with uniform incident field (yellow line), respectively. The results from both models show excellent agreement except a constant multiplier and this is acceptable since MoS_2 will not react to incident E_z and all responses are confined to be in-plane.

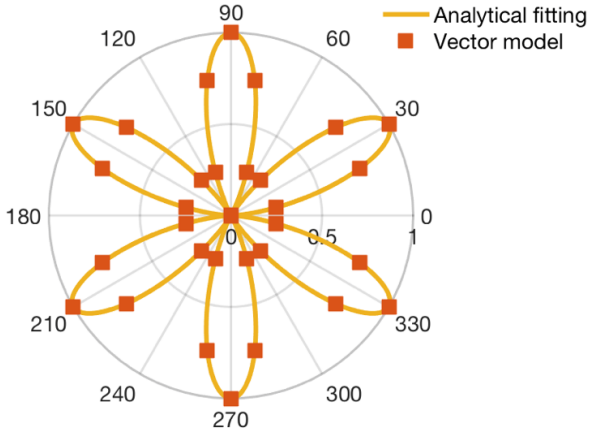

Figure 2.16 Polarization pattern of monolayer MoS_2 using different models. Y-polarized SH intensity of MoS_2 simulated form the Vector model by considering spatially varying incident field at focal plane (orange dots) and from an analytical model fitting (yellow line).

Next, we use the Vector model developed above to simulate the SH response from tBLG. For overall SH intensity comparison between MoS_2 and tBLG, there is no polarizer before the detector and intensities are normalized by the signal from MoS_2. Plots in Figure 2.17 are the angle-dependent SH intensity from tBLG with different values of χ_{xyz}. χ_{xxx} is chosen to be 100 times smaller than χ_{xyz} based on DFT results. Although there is no analyzer, angle-dependent SH intensity reveals the interference between different nonlinear tensor components agrees with our experimental observations (Figure 2.7b-2.7d).

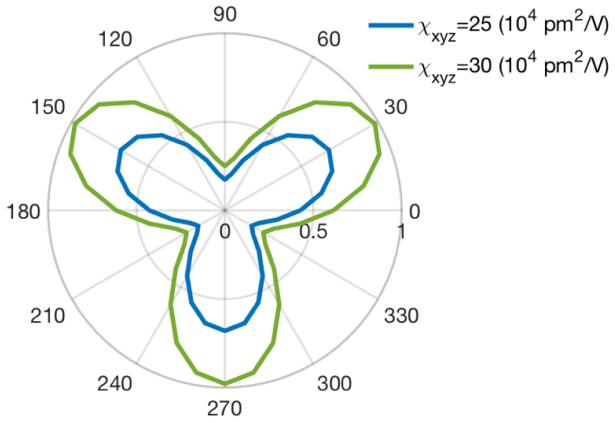

Figure 2.17 Simulated angle-dependent SH intensity of tBLG using the Vector model. Angle-dependent SH intensity distribution of tBLG without the analyzer. χ_{xyz} is chosen to be $25 \times 10^4\ pm^2/V$ (blue curve) and $30 \times 10^4\ pm^2/V$ (green curve) in the Vector model respectively. χ_{xxx} is set to be 100 times smaller than χ_{xyz}.

For the SH intensity comparison in Figure 2.5b, both MoS_2 and 6° tBLG are excited by 1064nm CW laser and the collected maximum SH intensity are comparable. The excitation for MoS_2 is off-resonant with susceptibility around 0.7×10^4 pm^2/V. On the other hand, the excitation is resonant for 6° tBLG and as shown in Figure 2.17. Since the susceptibility of tBLG should be around 28×10^4 pm^2/V, to achieve comparable values, the susceptibility for resonantly excited tBLG should be on the same order of resonantly excited TMDC system. The discrepancy of estimated values of tBLG susceptibility from a simple analytical model (3 (10^4 pm^2/V)) and from the Vector model (28 (10^4 pm^2/V)) not only uncovers the role of E_z enabled by the high-NA objective but also discloses the necessity of the Vector model to analyze the observed SH signal for our case.

2.7 Resonantly enhanced SHG response

Previous works have demonstrated the strong enhancement of G and R band intensity when the energy of laser matches those E_{vHs} in tBLG. By sweeping the incident wavelength and fixing the twisting angle, a clear trend can be obtained by fitting with second or third-order time-dependent perturbation theory[69]. In order to demonstrate the tunable nonlinear response of the tBLG system, here we choose the reverse process, that is, fixing the incident wavelength and sweeping the twist angle, which also give a similar trend due to the resonance matching mechanism.

The enhancement of Raman G peak of tBLGs can be described by second order time dependent perturbation[42]:

$$\frac{I_G}{I_{SLG}} = \left| \frac{M}{(E_{inc} - E_{vHs} - i\gamma)(E_{inc} - E_{vHs} - \hbar\omega_G - i\gamma)} \right|^2$$

In our case, E_{inc}(energy of incident photon) and $\hbar\omega_G$(energy of G phonon) is fixed and E_{vHs} is varied. By assuming M and γ are constant across all samples and using least square to fit the data in Figure 2.18a, we obtain the solid yellow curve. We found $M = 0.3318 \pm 0.00867$ and $\gamma = 0.2002 \pm 0.345$ consistent with results obtained in Ref 10. The Raman G peak shows pronounced enhancement when E_{vHs}=2.23eV with twist angle to be around 12°, which is consistent with other reports when incident wavelength is swept[42,70].

Next, we collected the SHG at 392.5nm from all tBLG samples with different twist angle while keeping the incident wavelength at 785nm. High efficiency of SHG is observed when the E_{vHs} is around 1.58eV and 3.16eV as shown in Figure 2.18b with the corresponding twist angles to be about 8° and 20° respectively[42,70]. Such a dependence of SHG intensity on varying vHs levels indicates resonant SHG processes[71,72], where the SHG is enhanced when one or two incident photons are in resonance with electronic transitions in tBLG. Note that the dependence of E_{vHs} on twist angle does not follow the relation E_{vHs}=3.9sin(3θ) exactly, especially at large twist angles.

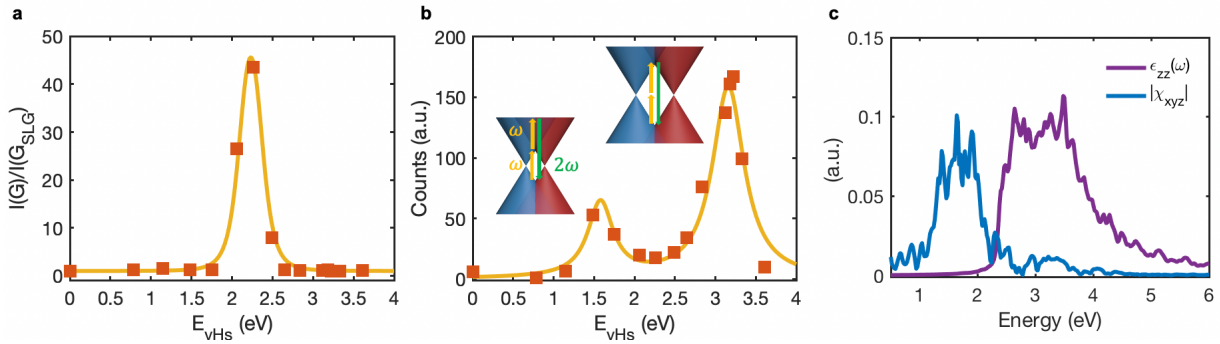

Figure 2.18 (a) Raman G peak enhancement with different twist angles using 532nm laser. The orange dots are experimental results and the yellow curve is the G peak enhancement fitting based on the work[42]. (b) Normalized SHG signal of tBLGs with different twist angles under 785nm excitation. The orange dots are experimental data and the yellow curve is the fitting result. The insets correspond to 1- and 2- photon resonant SHG processes. (c) Spectrum of the imaginary part of linear permittivity in z-direction (purple) and the absolute value of χ_{xyz} (blue) of a 21.8° tBLG.

For the resonant transitions involved in the SHG process, we use a coherent superposition of second-order nonlinear susceptibility of 1- and 2-photon resonances[73,74]:

$$I(2\omega) \propto (\chi^{(2)})^2 \propto \left(\frac{f_1 \exp(i\varphi_1)}{(E_{inc} - E_{vHs} + i\Gamma_1/2)} + \frac{f_2 \exp(i\varphi_2)}{(2E_{inc} - E_{vHs} + i\Gamma_2/2)}\right)^2$$

where E_{inc} is the energy of incident light, E_{vHs} corresponds to the energy of vHs transitions in tBLG. In this work, we are using different twist angles to demonstrate the tunable nonlinear response of the tBLG system, therefore E_{inc} is fixed to be 1.58eV and E_{vHs} is swept from 0 to 4eV. The phase value φ_i does not play an important role here because the two resonant frequencies are well separated. f_i and Γ_i (i=1, 2) determines the amplitude and the bandwidth of resonant peaks respectively. The solid line in Figure 2.18b is the fitting result which shows that 1-photon resonance is around 1.573eV and 2-photon resonance is around 3.158eV in line with expectations.

Considering the computational difficulty to calculate the susceptibility of tBLG with small twist angles[42,43], we compare the imaginary part of linear permittivity in the z-direction with the dominant tensor component, χ_{xyz}, of a 21.8° tBLG in Figure 2.18c. $\varepsilon_{zz}(\omega)$ shows a dominate peak around E_{vHs} for a 21.8° tBLG. Although decaying in the low-frequency range, it is still finite at halved E_{vHs}. Besides, the involvement of dipolar response in z-direction validates the non-vanishing χ_{xyz} and the spectral overlap supports both resonant processes.

The novel and tunable low dimensional nonlinear material demonstrated here can be readily integrated onto silicon waveguides and resonators for integrated nonlinear optics applications. The large χ_{xyz} not only allows the strong interaction with usually unaccessible TM modes, but also enables more efficient phase matching of the nonlinear process. More advanced control such as gating in tuning the nonlinear behavior of tBLG can further deepen our understanding of the material system as well as enlarge the working bandwidth of integrated nonlinear platform.

In summary, we observed the twist-angle-dependent SHG in inversion-symmetry-broken tBLGs. The extracted susceptibility of on-resonant tBLG is comparable to on-resonant monolayer MoS_2 and remains non-vanishing over a range of angles. The tunable SHG achieved here differs from previous nonlinear engineering work that based on the fixed susceptibility dispersion[72]. Enabled by tBLG system, determinant factors of SHG response such as underlying symmetry and electronic structure can be readily changed just by twisting. Combined contributions of dominant chiral tensor component, χ_{xyz} and other non-chiral ones give rise to polarization patterns with 3-fold symmetry which potentially allow an easier identification of the high symmetry axes in tBLG samples compared to Scanning Tunneling Microscopy or Transmission Electron Microscopy methods when all tensor components are already known. The involvement of the z-polarized field and the large magnitude of χ_{xyz} we found here provide a new perspective to explore the exciton levels around vHs transition frequency. Moreover, the existence of χ_{xyz} unravels the possible piezoelectric properties which may motivate further mechanical studies on tBLG systems. Due to the strong interlayer coupling between artificially stacked graphene, we also expect exotic nonlinear behavior from multi-layer stacked graphene and other vdW materials with more complicated crystal symmetries[43,75].

Chapter 3: Photonic Rashba-Dresselhaus spin-orbit coupling (SOC)

3.1 Review of photonic Rashba and Dresselhaus SOC realizations

Similar to the case of charged particles in an external magnetic field, the Hamiltonian of an engineered systems under artificial gauge field, such as ultracold atomic gases, photonic lattices and mechanical oscillators, are modified by a gauge potential $\boldsymbol{A}$[76]. Depending on the exact schemes implemented, the form of gauge potential and the resultant dynamics of the system varies. In photonics, for example, uniform artificial magnetic fields can be achieved in 2D lattices with broken time-reversal symmetry or in resonator arrays with asymmetric coupling where both Hofstadter butterfly spectrum and topological edge states can be observed[77–83]. Time dependent gauge potential $\boldsymbol{A}(t)$ which originally denotes the external electric field in electronic system was synthesized in a helical waveguide array[84–87]. Artificial gauge potential resembles spin-orbit coupling (SOC) can be expressed in terms of Pauli matrices: $\boldsymbol{A}(\sigma_x, \sigma_y, \sigma_z)$. With the proper definition of pseudo-spin, realization of Dresselhaus SOC in semiconductor microcavities due to TE-TM splitting[88,89], strong SOC enabled topological insulators in bianisotropic metamaterial lattice[90,91] and coupled resonators[92,93] expand the possible forms of artificial gauge field.

Conventional Rashba-type SOC usually arises at the surface or in confined 2D electron systems under a perpendicular electric field and is accompanied by spin-splitting in the band structure[94]. Due to the small atomic number of carbon atoms, the intrinsic Rashba SOC is usually weak in emergent Van der Waals materials such as graphene and graphene-like materials[95,96]. Efforts in recovering and strengthening intrinsic SOC response in graphene such as alkali adsorption and graphitization of Ni followed by intercalation of Au have been made[15,97–99]. Nevertheless, it still remains difficult to clearly resolve spin-split bands and distinguish different SOC contributions which impede the practical application in spintronics. Similarly, Dirac points splitting and associated potential topological phenomenon in gated BP due to Rashba SOC are predicted but the distinguishability of spin-dependent features is still beyond the capability of current techniques[100–102]. By implementing these subtle SOC related physics in a larger scale, for instance, in photonic resemblances of graphene or black phosphorus (BP), better understanding of interaction between Bloch states and gauge fields will be gained and more unexplored topological properties associated with Rashba-type SOC will be observed.

Optical analog of Rashba effect has been demonstrated in inclined waveguide array as shown in the Figure 3.1[103]. By exploring the paraxial wave propagation in 1D waveguide array, the analogue between wave equation and Schrodinger equation is established. The profile of refractive index distribution plays the rule of potential. The resulting dispersion relation, $\beta = 2tcos(ka)$, resembles those of 1D atomic chains. By tilting the waveguide array, an instantaneous change of index profile is introduced. The k dependent term in the dispersion appears after performing a coordinate transformation of inclined waveguides to the reference frame: $\beta = 2tcos(ka - \eta k_0 a) + \eta k$. Constructing a bilayer waveguide array with opposite tilting direction, the Hamiltonian becomes nontrivial with finite gauge field (Figure 3.1c). The pseudospin degree of freedom is represented by the top and bottom array modes. However, the above setting needs inclined waveguides with different tilting angles to maintain effective gauge field and thus cannot be readily applied to 2D realm with a uniform gauge field.

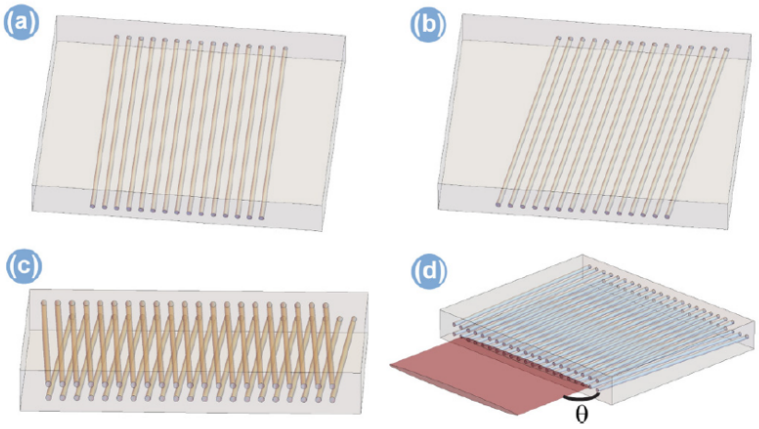

Figure 3.1. (a) A single 1D array of straight untilted waveguides. (b) A single array of tilted waveguides. (c) Two arrays, with the top one tilted to the left and the bottom one tilted to the right. (d) Illustration of the excitation method of the waveguide array. Figure adapted from[103].

On the other hand, the demonstration of Rashba-Dresselhaus spin-orbit interaction in the optical cavity filled with liquid crystal suggests another possibility to break inversion symmetry of the 2D continuum medium by controlling the anisotropic refractive index (Figure 3.2)[104–106]. In this case, the circular polarizations represent two spin states. The electric fields take the form of plane-wave as in a 1D cavity: $E(x,y,z) = E_k(z)e^{i(\boldsymbol{k}\cdot\boldsymbol{r}-\omega t)}$. Simplifying the Maxwell equation with permittivity tensor, the eigenequation for electric field is given by: $-\partial_z^2\boldsymbol{E} + \hat{A}\partial_z\boldsymbol{E} + \hat{B}_1\boldsymbol{E} = k_0^2\hat{B}_0\boldsymbol{E}$. The electric field can then be expanded by the orthonormal basis functions of the 1D cavity for two different polarization direction. It turns out that the interaction of orthogonally polarized modes with opposite parity give rise to a Hamiltonian with Rashba-Dresselhaus SOC. Therefore, a detailed tuning of the system parameter, for example the vertical source field, is needed to achieve the exact SOC interaction.

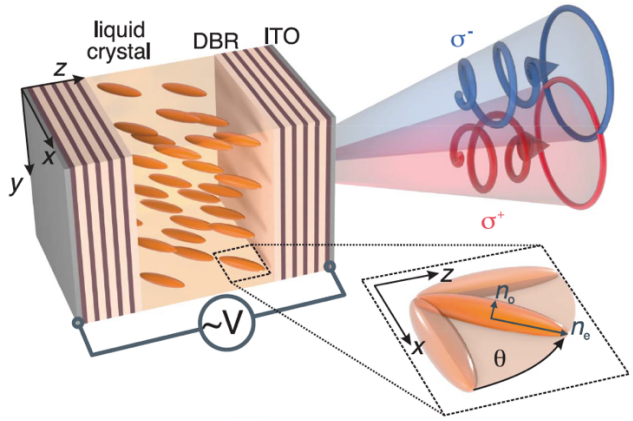

Figure 3.2. Rashba-Dresselhaus spin-orbit coupling in a liquid crystal–filled optical cavity. Figure adapted from[104].

In a more general birefringent platform without pseudospin designation, it has been shown that by introducing a complex coupling phase, artificial gauge field can also be realized[107]. The complex

coupling is enabled by birefringent background dielectric media as shown in Figure 3.3. As a result, the mode will accumulate phase along x for large k_z and the coupling now becomes directional. A natural consequence is the shift of the bands along k_x which resembles 'Rashba shifting'. The unnecessity of pseudospin definition permits further construction of a photonic Haldane model with vortex-like index distribution.

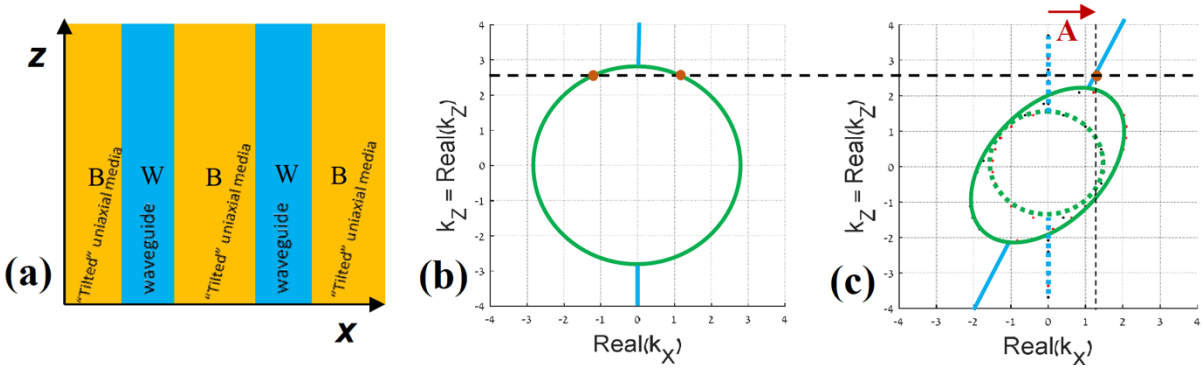

Figure 3.3 Gauge fields achieved by complex coupling of adjacent waveguides. (a) Schematics of the system. (b,c) Wavenumber diagram for plane wave solutions in the materials. Figure adapted from[107].

3.2 Gauge fields induced by tilted anisotropy

The direct relation between the anisotropic constitutive parameters and the direction/magnitude in a continuum medium can be revealed by considering field transformation[108,109]. Complementary to transformation optics, field transformation manipulates the polarization instead of the phase of propagating wave. Assuming that the system is two-dimensional with a mirror symmetry in x-y plane, the modes can be classified as decoupled TE and TM. The field transformation for the longitudinal field part has the following form:

$$\begin{pmatrix} E_z \\ iH_z \end{pmatrix} = \begin{pmatrix} \cos(k_0\phi) & -\sin(k_0\phi) \\ \sin(k_0\phi) & \cos(k_0\phi) \end{pmatrix} \begin{pmatrix} E_z^{(0)} \\ iH_z^{(0)} \end{pmatrix}$$

The k_0 is the wavenumber and will be different when the frequency varies. Field transformation with spatially varying ϕ keeps Maxwell's equation the same while the underlying medium has new forms of permittivity and permeability tensors:

$$\varepsilon = \begin{pmatrix} \varepsilon_{xx} & \varepsilon_{xy} & \partial_y\phi \\ \varepsilon_{yx} & \varepsilon_{yy} & -\partial_x\phi \\ \partial_y\phi & -\partial_x\phi & \varepsilon_{zz} \end{pmatrix}$$

$$\mu = \begin{pmatrix} \varepsilon_{xx} & \varepsilon_{xy} & -\partial_y\phi \\ \varepsilon_{yx} & \varepsilon_{yy} & \partial_x\phi \\ -\partial_y\phi & \partial_x\phi & \varepsilon_{zz} \end{pmatrix}$$

The ε_{xz} and ε_{yz} are now the gradient of ϕ and has the form of the pure gauge field. By writing the pseudospin states in terms of TE and TM modes: $\psi_{\pm} = E_z \pm H_z$, the Maxwell equation can be written as the form similar to the Schrodinger equation:

$$(\nabla \pm ik_0 A) \cdot \frac{1}{m} \cdot (\nabla \pm ik_0 A)\psi + k_0^2 \varepsilon_{zz} \psi = 0$$

A direct consequence compared to the case before the transformation is that the dispersion surface corresponding to different pseudospin states will split and move oppositely: $\boldsymbol{k} \to \boldsymbol{k} \pm k_0 \boldsymbol{A}$[110]. The above derivations are formalized in a continuum media and the direct connection between spatially varying gauge field and off-diagonal tensor elements are established. On the other hand, in a periodic lattice setting with anisotropic constituting materials, it is not clear what the form of induced gauge field will be due to off-diagonal terms.

In the following, we start from a honeycomb lattice with anisotropic permittivity and permeability. The simulation results give a similar splitting behavior due to gauge field. However, after the plane wave expansion around high symmetry point, we find that the induced gauge field now has a form of Rashba-Dresselhaus SOC. Furthermore, the clear relationship between the 'tilted' constitutive parameters and the direction of pseudo-spin polarized bands is revealed as well.

3.3 Effective magnetic field distribution

Similar to the case of charged particles in an external magnetic field, the Hamiltonian of an engineered systems with spin-orbit coupling (SOC) can also be considered as the coupling between photonic pseudo-spin and an effective magnetic field[111,112]. Shown in Figure 3.4 are k-dependent effective magnetic fields in the reciprocal space for different type of SOC. The k-varying field indicates that spin of eigenstates is also varying in k space which lays the foundation for spin separation and spin-charge conversion[113]. In Figure 3.4, two panels on the left list the expressions and show the distribution of effective magnetic field for Rashba SOC and Dresselhaus SOC.

Different form conventional individual Rashba and Dressslhaus SOC, the SOC enabled by tilted anisotropy consists of equally weighted Rashba and Dresselhaus SOC[104,114,115]. Consequently, as shown in the right panel of Figure 3.4, the spin has only two possible states by definition and the corresponding k can be changed by the relative phase between α and β which is equivalent to a rotation of the energy contour. Based on the tilted anisotropy and the induced effective magnetic field, it is possible to realize a photonic version of the spin Hall effect[112,116,117].

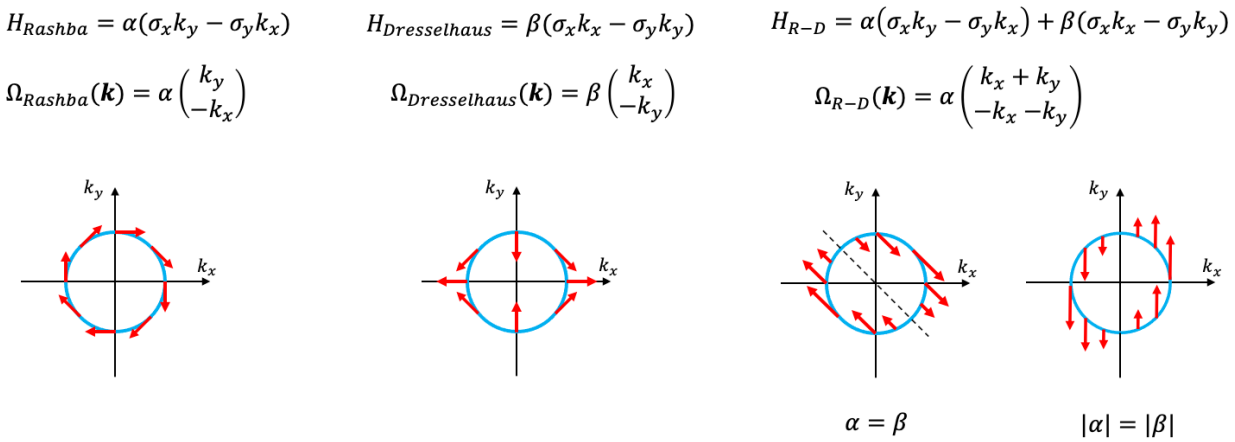

Figure 3.4 Expressions and field distribution of Rashba, Dresselhaus and Rashba-Dresselhaus type effective magnetic field.

3.4 Implementation of Rashba-Dresselhaus SOC in 2D photonic analogues

In order to include the anisotropic material properties, the constitutive parameters in the Maxwell equation takes the more general tensor form:

$$\varepsilon = \begin{bmatrix} \varepsilon_d & \varepsilon_{xy} & \varepsilon_{xz} \\ \varepsilon_{xy} & \varepsilon_d & \varepsilon_{yz} \\ \varepsilon_{xz} & \varepsilon_{yz} & \varepsilon_d \end{bmatrix}, \mu = \begin{bmatrix} \mu_d & \mu_{xy} & \mu_{xz} \\ \mu_{xy} & \mu_d & \mu_{yz} \\ \mu_{xz} & \mu_{yz} & \mu_d \end{bmatrix}$$

Since the systems under consideration are time-reversal symmetric, there are only three independent off-diagonal components (ε_{xy}, ε_{xz} and ε_{yz}), same for μ. By setting the diagonal elements of both permittivity and permeability to be equal: $\varepsilon_d = \mu_d$ and all the off-diagonal ones to be zero, a double spin degenerate Dirac cone is guaranteed at K point in the isotropic 2D honeycomb lattice, schematically shown in Figure 3.5a and 3.5b.

Assigning none-zero and opposite values to one of the corresponding off-diagonal elements of ε and μ, for example $\varepsilon_{yz} = -\mu_{yz} = 2$, results in a clear separation of spin-polarized Dirac cones along k_x direction (Figure 3.5c and 3.5d). Figure 3.5e shows the first Brillouin zone of honeycomb lattice and the positions of degenerate Dirac point (gray) and those displaced ones after introducing the anisotropic terms (blue and red). The spin states for the numbered modes in Figure 3.5d are verified by evaluating the phase difference between E_z and H_z fields (Figure 3.5f)[90]. The left-moving spin-down and the right-moving spin-up bands preserve the Dirac cone feature (Figure 3.5d) and form a pair of Type-I tilted Dirac dispersion.

According to the gauge transformation theorem developed in[109], the above case in which ε_{yz} and μ_{yz} have the same magnitude but opposite sign corresponds to a real-space gauge field along x direction in a continuum medium. In the following we will theoretically show that the employment of anisotropy in the periodic lattice configuration leads to an artificial Rashba-Dresselhaus type SOC gauge field. Although spin-splitting is observed in both scenarios, the interaction between orbital degree of freedom associated with Bloch states and induced gauge field considered here

gives us opportunity to emulate and further uncover the subtle SOC-related physics which are difficult to be detected in electronic systems.

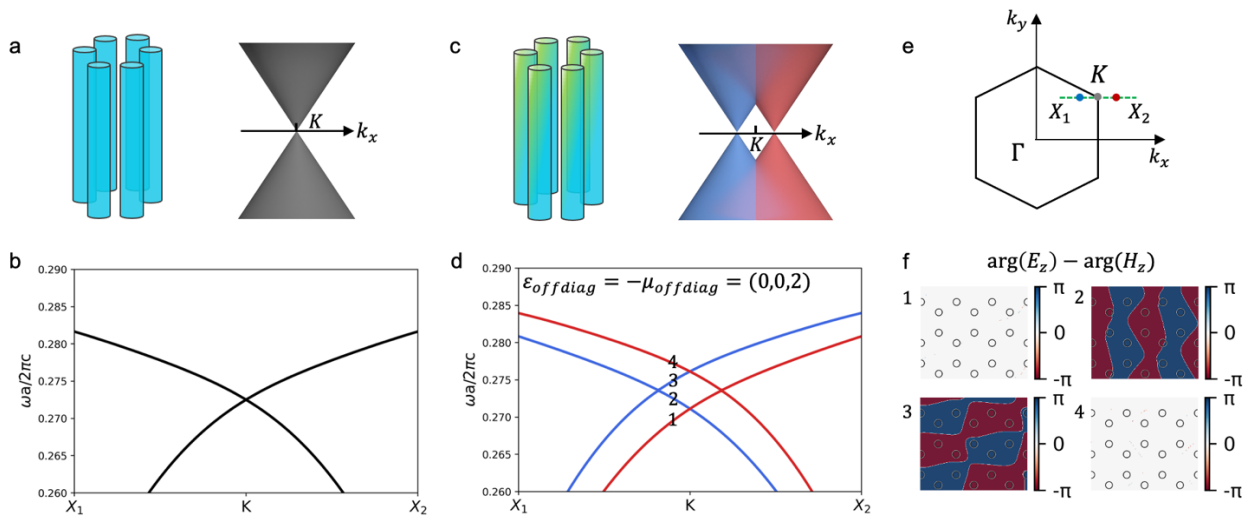

Figure 3.5 (a) Schematic of a honeycomb lattice with isotropic constitutive parameters and the band structure with doubly degenerate Dirac cones. (b) Simulated band structures around K point. (c) Schematic of a honeycomb lattice with anisotropic constitutive parameters and the band structure with spin-polarized Dirac cones. (d) Simulated band structures around K point with nonzero $\varepsilon_{yz}(\mu_{yz})$. (e) Illustration of the shifting of spin-polarized Dirac cones. The blue (red) dot represents the spin-down (-up) polarized Dirac point. (f) The phase distributions for the four bands numbered in (d).

3.5 Plane-wave expansion method for deriving system Hamiltonian

Starting from the most general Maxwell's equation with only none-zero ε_{yz} and μ_{yz}, the two spin states defined as $\psi_{\pm} = E_z \pm H_z$ are decoupled and satisfy:

$$\omega^2\left(\varepsilon_d - \frac{\varepsilon_{yz}^2}{\varepsilon_d}\right)\psi_{\pm} + \frac{\partial}{\partial x}\left(\frac{1}{\varepsilon_d}\frac{\partial \psi_{\pm}}{\partial x}\right) + \frac{\partial}{\partial y}\left(\frac{1}{\varepsilon_d}\frac{\partial \psi_{\pm}}{\partial y}\right) = i\omega\frac{\varepsilon_{yz}}{\varepsilon_d}\frac{\partial}{\partial x}\psi_{\pm} + i\omega\frac{\partial}{\partial x}\left(\frac{\varepsilon_{yz}}{\varepsilon_d}\psi_{\pm}\right)$$

Rearranging the terms in the above wave equation gives a form similar to the Schrodinger equation with canonical momentum. To find the low energy Hamiltonian of the anisotropic system around K point with periodical modulation, fields and constitutive parameters are expanded in plane waves[20,90]. The low-energy Hamiltonian of the four spin-polarized relevant states can be written as:

$$H = \left(\delta k_x \sigma_x + \delta k_y \sigma_y\right) v_D + 2\omega\theta\delta k_x s_z + K\omega\theta\sigma_x s_z$$

where σ and s are Pauli matrices representing the different sublattice and spin states. θ is fixed and related to the Fourier components of the periodically distributed ε.

The energy dispersions of the two spin-polarized states around K can be obtained from the above equation:

$$E_+(\delta k) = 2\omega\theta\delta k_x \pm \sqrt{(\delta k_y v_d)^2 + (\delta k_x v_d + \omega K\theta)^2}$$

$$E_-(\delta k) = -2\omega\theta\delta k_x \pm \sqrt{(\delta k_y v_d)^2 + (\delta k_x v_d - \omega K\theta)^2}$$

The dispersions are featured by a symmetric pair of tilted Dirac cones and the Dirac points for different spin states are shifted along k_x and $-k_x$ direction respectively (Figure 3.5d). The second term in the Hamiltonian can be identified as Spielman's form of equal Rashba and Dresselhaus SOC after a proper coordinate transformation[104].

For the case with none-zero $\varepsilon_{yz}(\mu_{yz})$, the second and third term in Hamiltonian combined leads to the overall shift along k_x direction. The magnitude of shifting and the associated tilting obtained by the proposed method are directly related and controlled by the off-diagonal to diagonal element ratio $\frac{\varepsilon_{yz}}{\varepsilon_d}$, which is embedded in the parameter θ. In the following we will show the generality in emulating Rashba effect with controllable spin-splitting direction.

Under the same methodology, by assigning $\varepsilon_{xz}(\mu_{xz})$ none-zero values, spin-polarized Dirac cones are expected to shift along k_y direction. As shown in Figure 3.6a, the doubly degenerate Dirac cone at K point in the isotropic case now become spin polarized and the spin-up (spin-down) states and move to Y_1 (Y_2). The energy dispersion along Y_1-K-Y_2 and X_1-K-X_2 are shown in Figure 3.6b and 3.6c in contrast to the case in Figure 3.5d. Although in both cases, the constitutive parameters of the medium in the principal coordinates system are the same: $\varepsilon_d = \mu_d = (10,12,14)$, the contrasting behavior indicates the dependence of shift, $\delta\boldsymbol{k}$**,** on the 'tilting' angle of anisotropic tensors.

Like the vector addition in 2D coordinate system, the combination of finite $\varepsilon_{xz}(\mu_{xz})$ and $\varepsilon_{yz}(\mu_{yz})$ allows two spin-polarized Dirac cones to move oppositely along arbitrary directions around K points. For example, the 'additive' results from Figure 3.5e and Figure 3.6a satisfied by having $\varepsilon_{xz} = \varepsilon_{yz} = -\mu_{xz} = -\mu_{yz} = 2$, are the movement of spin-down and spin-up states toward X_1^u and X_2^d respectively (Figure 3.6d-3.6f). The flexibility demonstrated here is enabled by the 'tilting' freedom which is absent in solid-state crystals with fixed symmetries.

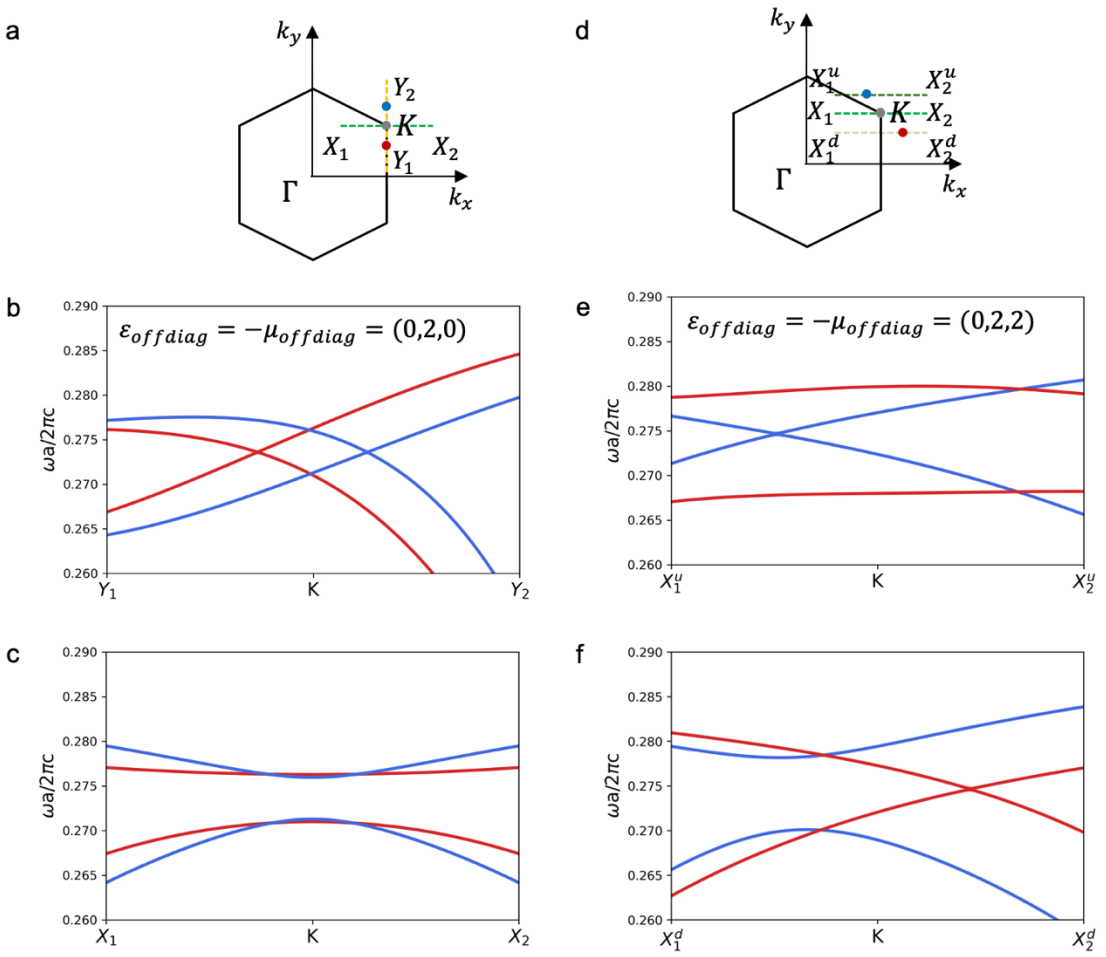

Figure 3.6 (a) Schematic of the splitting of spin-polarized bands along k_y direction with nonzero $\varepsilon_{xz}(\mu_{xz})$. (b and c) Simulated band structures of shifted bands along k_y and k_x direction respectively. (d) Schematic of the splitting of spin-polarized bands along k_y direction with nonzero $\varepsilon_{xz}(\mu_{xz})$ and $\varepsilon_{yz}(\mu_{yz})$. (e and f) Simulated band structures of shifted bands along k_x direction with different k_y value.

3.6 Applicability for various 2D photonic systems

Next, we apply the developed method to reproduce the band structures of monolayer BP, gated BP and transition metal monochalcogenide (MX) with corresponding SOC induced splitting in the photonic realm. Although, there have been theoretical predictions on the spin-polarized bands due to intrinsic SOC in solid-state systems, the associated phenomena are still beyond the current detection limit[100,101]. On the other hand, photonic analogs are not only capable of enhancing these delicate spin-splitting behavior, but also acts as test bed for potential spintronic applications.

In the following, we adopt the two-band model for BP and MX without losing the essential features[118]. As shown in Figure 3.7, there are four atoms in the puckered monolayer BP. Therefore,

in the rectangular first Brillouin zone, there are in total four bands with an energy gap at Γ point (shown in Figure 3.8c).

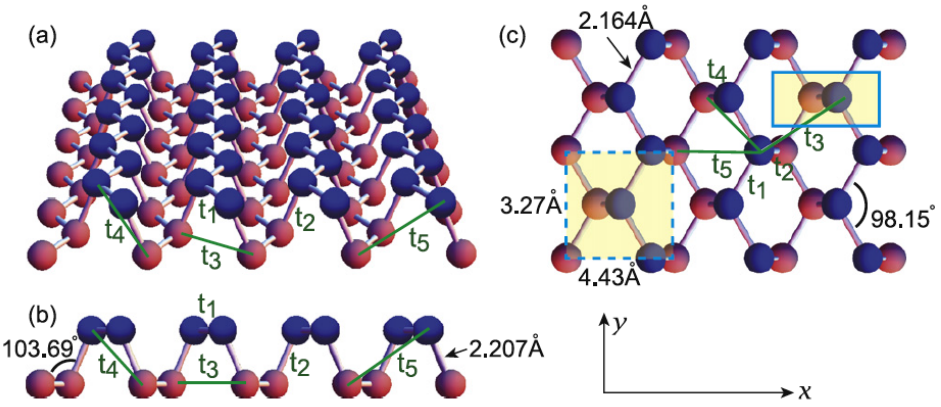

Figure 3.7. Illustration of the structure and the transfer energy of phosphorene. (a) Bird eye's view. (b) Side view. (c) Top view. Red (blue) balls represent phosphorus atoms in the upper (lower) layer. A dotted (solid) rectangular denote the unit cell of the four-band (two-band) model. The parameters of the unit cell length and angles of bonds denoted. Figure adapted from[118].

Due to the D_{2h} symmetry invariance, it is possible to reduce the above four-band model to a two-band model. When looking from the top and the bottom of puckered layer, the two views are the same. From a 2D photonics view, the directionality of the bonds such as t_2 and t_4 can be simplified as an in-plane coupling. Thus, we only need to consider two atoms in one unit cell. As a result, the Brillouin zone of the two-band model becomes hexagonal shown in Figure 3.8b. The original energy bands can be achieved by folding back the hexagonal Brillouin zone and now the M point in two-band model is equivalent to the Γ point in the four-band model (Figure 3.8d).

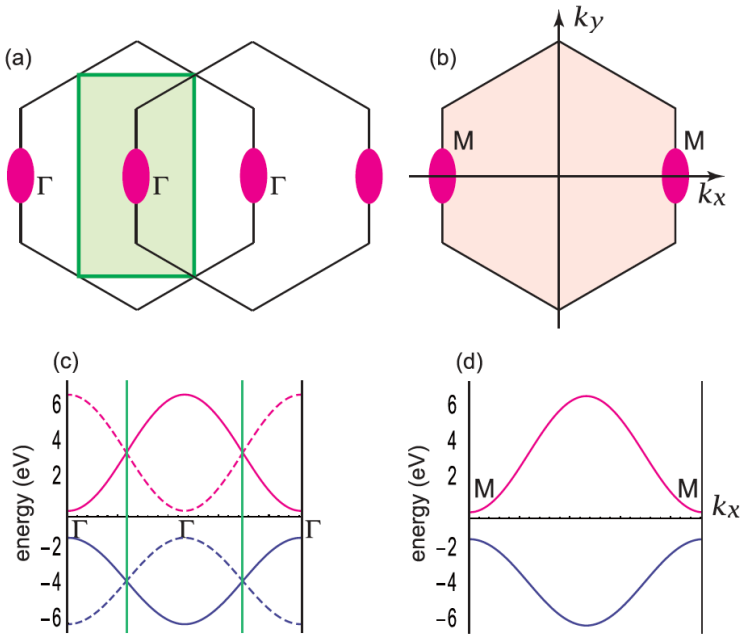

Figure 3.8 (a) The Brillouin zone is a rectangular in the four-band model, which is constructed from two copies of the hexagonal Brillouin zone of the two-band model. A magenta oval denotes a Dirac cone present at the Γ point. (b) The Brillouin zone is a hexagonal in the two-band model. A magenta oval denotes a Dirac cone present at the M point. (c) The band structure of the four band model, which is constructed from two copies of that of the two-band model. (d) The band structure of the two-band model. Figure adapted from.

It is therefore straightforward to represent photonic BP by a strained honeycomb lattice[119,120]. As shown in the Fig. 3.9a, the monolayer BP represented by a strained honeycomb lattice opens an anisotropic bandgap at M point similar to the original one at Γ point. The isotropy of materialization ensures the degeneracy of two spin states. Reducing the effective stain leads to the case of gated BP (Figure 3.9c) with the emergence of a Dirac point located at K_D. MX lattice is obtained by breaking the sublattice symmetry which opened a gap at the previous Dirac point (Figure 3.9e)[121]. Introduction of $\varepsilon_{yz}(\mu_{yz})$ to the above three systems lift the degeneracy of bands and shifts different spin states oppositely while maintaining the topology of the original bands (Figure 3.9b, 3.9d and 3.9f).

The Dirac cones in BP has been experimentally observed in the band-inverted regime by applying surface doping[100,119]. The intrinsic spin-orbit coupling in BP makes each Dirac point split into a pair of Weyl points instead of opening a gap. The space-time inversion symmetry is identified to stabilize these Weyl points located off the high-symmetry axes and possible Fermi arcs are predicted to connect the pair of 2D Weyl points. However, due the extremely small splitting, it is difficult to explore these intriguing features in solid-state BP system. On the other hand, the splitting achieved in the photonic BP share similar traits (Figure 3.9d) and provide a potential platform for the study of 2D Weyl photonics[122].

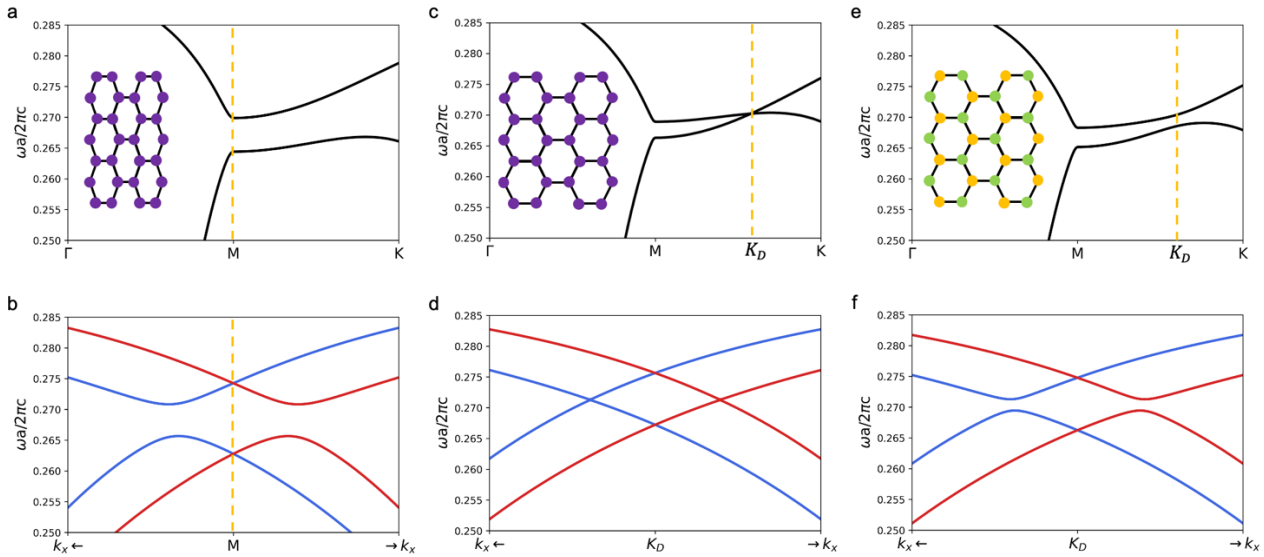

Figure 3.9 (a) Band structure and lattice configuration of the two-band model BP. (b) Band structure of two-band model BP with Rashba-Dresselhaus SOC. The yellow dotted line indicate the center of the splitting. (c and d) Strained BP case. (e and f) MX case with broken sublattice symmetry.

3.7 Local berry phase distribution for different 2D photonic lattices

Graphene lattice with sublattice symmetry breaking possesses local berry curvature[21,123]. As shown in Figure 3.10a, a small gap opens at K point and the local berry curvature distribution is plotted for the area indicated by green rhombus. Although, the integration of local berry curvature over the whole Brillouin zone is zero, finite local values concentrated at K and K' are responsible for the valley Hall effect. Only when the sublattice symmetry-breaking (Δε) is small, the valley Chern number is an integer[124]. As Δε becomes larger for the honeycomb lattice, the distribution of local berry curvature broadens as shown in Figure 3.11. At the point when the berry curvature from different valleys with opposite values overlap, the valley Chern number deviates from the quantized value.

In addition to the variation of Δε[123,125], the change of lattice structure, for example adding strain to the staggered graphene, the local berry will evolute accordingly[126]. Shown in Figure 3.10b, the moderately strained graphene with an energy gap between M and K point represents a photonic MX. The center of local berry curvature of it moves from K to the position of new band gap compared to the unstrained case. If the strain is even larger, the bandgap will be located at M which resembles a staggered BP system and the broadened berry curvature distribute closer to the M point. The results indicate that valley Hall or kink state might also exist in the photonic MX and BP systems. Furthermore, if Rashba-Dresselhaus SOC is introduced, uncoupled spin-up and spin-down states will inherit the same valley properties as discussed above. The detail of Berry curvature calculations can be found in the Appendix.

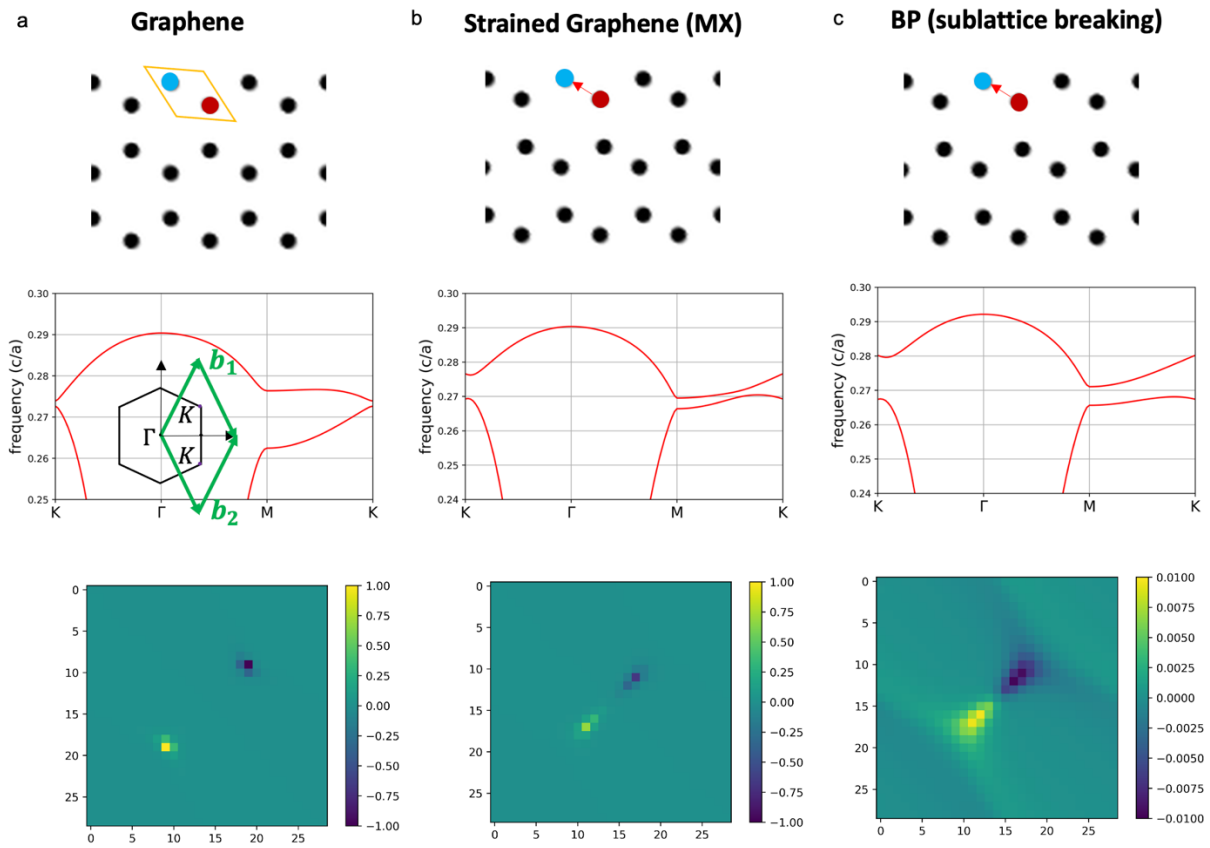

Figure 3.10 (a) Schematics of the 2D graphene lattice with broken sublattice symmetry and its band-structure and local berry phase distribution for two-dimensional graphene. (b) Strained staggered graphene case representing a MX system. (c) Staggered graphene lattice with higher stain representing an BP with staggered on-site potential.

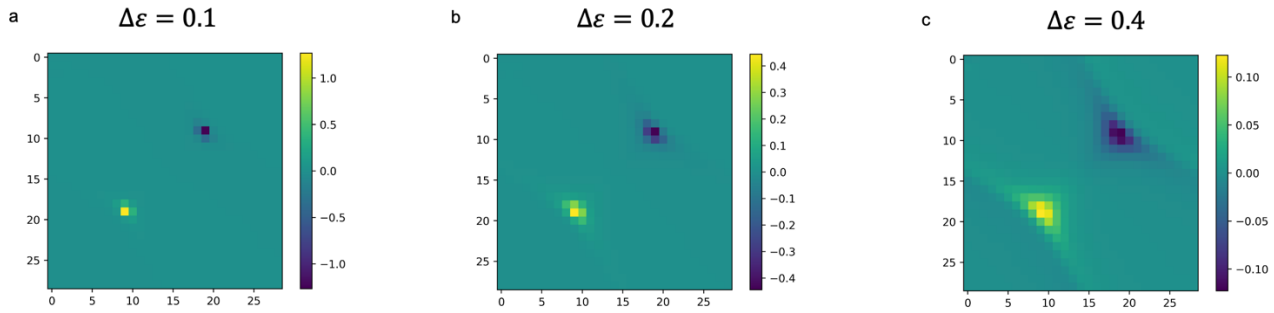

Figure 3.11 Local berry phase distribution of staggered graphene lattice with different magnitude of sublattice symmetry breaking $\Delta\varepsilon$.

3.8 Emergent photonic spin-polarized edge states and spin Hall effect

As it has been both theoretically and experimentally demonstrated that the zigzag edge of graphene holds edge states (Figure 3.12a)[127,128], it is natural to generalize it to the same honeycomb system when different spin states are considered.

The implementation of Rashba-Dresselhaus SOC successfully split both bulk and edge bands shown in the bottom panel of Figure 3.12a. The universal splitting ensures that all spin-up states move towards positive k_x direction, and all spin-down states move towards negative k_x direction. As a result, there are two spin-polarized edge states on each zigzag edge.

For wavenumbers around k_- and k_+, it is clear that in these limited range of wavenumbers the edge states are purely singly spin-polarized with spin-up states propagating to the left and spin-down states propagating to the right. The field profile and phase distribution at k_- and k_+ are plotted in Figure 3.12b. The localization of $|E_z|$ at the ribbon edge guarantees its edge state nature and the phase differentiate two distinct spin polarization.

The spin-momentum locking observed here is similar to the edges in Z_2 topological insulator[129]. However, the scatter-immune property is absent here because the scattered wavenumbers is not guaranteed to lie inside the singly spin-polarized range and back reflection is allowed. Besides edge states, Rashba-Dresselhaus SOC also enables spin-momentum locked propagating of bulk modes.

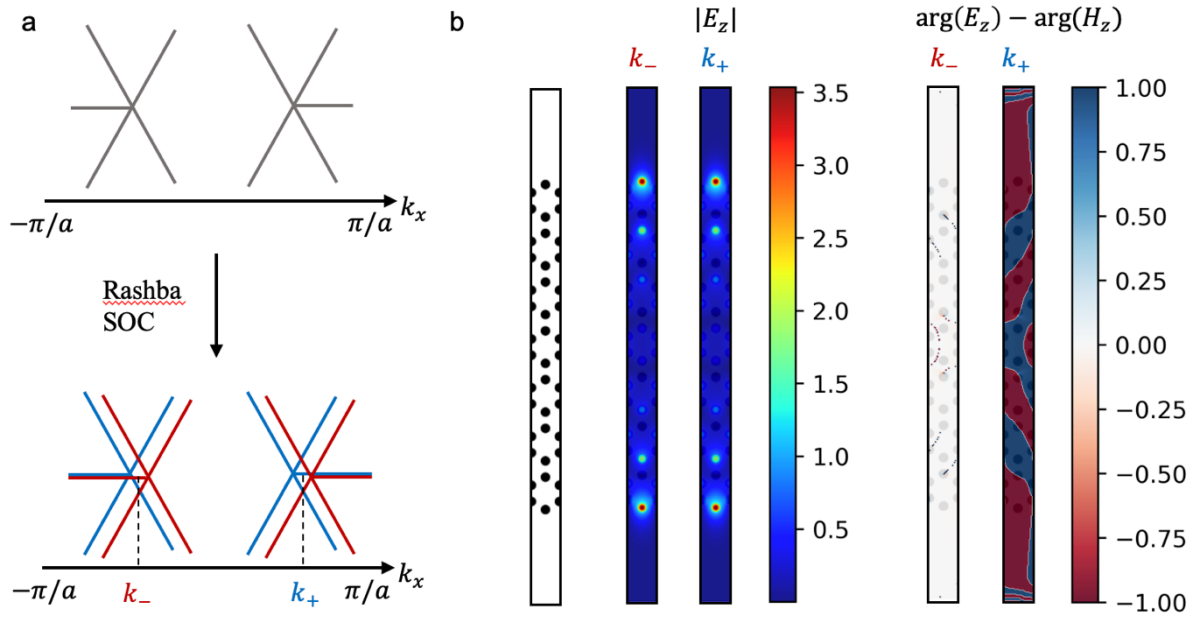

Figure 3.12 (a) Top: Schematic band structure of graphene ribbon with zigzag edge without SOC. Bottom: Schematic band structure of graphene ribbon with zigzag edge with Rashba-Dresselhaus SOC. Wavenumber k_-(k_+) indicate the region where there is one spin-polarized edge state. (b) Left: The ribbon structure used in the simulation. Right: $|E_z|$ field and phase distribution of the edge states at k_- and k_+ respectively.

Figure 3.13a shows the band splitting due to Rashba-Dresselhaus SOC near the K point. The bandgap opens by breaking the sublattice symmetry. As denoted by the green dashed line, the spin-polarized states of highest energy in the valence bands shift oppositely around the K point. The shifting is illustrated in Figure 3.13b with blue and red dots representing the states having same energy but different spin polarization. On one hand, the spin-down state moves to the left of K point with a positive sign of k_x. On the other hand, the spin-up state moves to the right of K which is equivalent to the state with a negative sign of k_x (red dot on the left). Both states considered have the same k_y component. Therefore, if we excite the system using a spinless dipole source at this specific energy, counter-propagating spin-polarized waves are expected (Figure 3.13c).

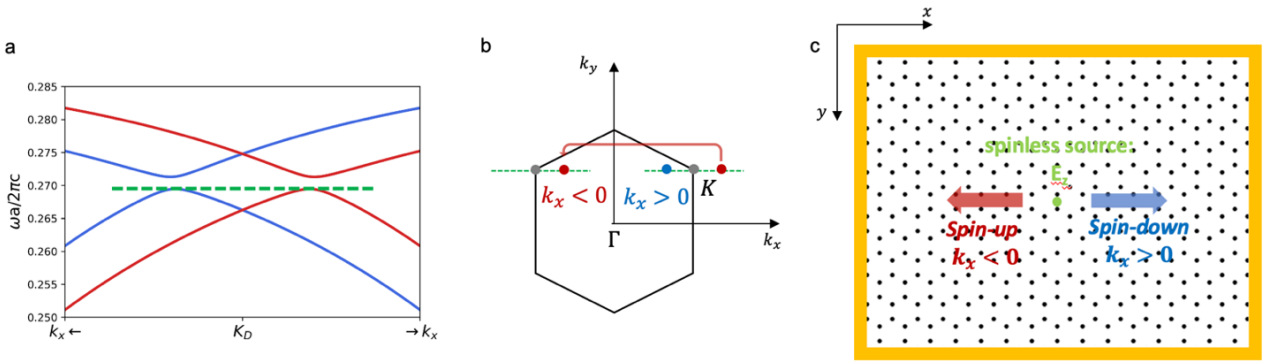

Figure 3.13 (a) Splitted bands due to Rashba-Dreselhaus SOC near K_D point. Green dashed line indicates the energy of the top of valence band. (b) Schematics of the splitting in the first Brillouin

zone. (c) Illustration of the counter-propagating spin-polarized bulk waves under a spinless source excitation.

As shown in Figure 3.13c, the graphene lattice with staggered potential is surrounded by perfectly mathched layers to reduce reflection at all boundaries. A spinless source with E_z polarization is placed at the middle which can excite both spin-up (E_z +H_z) and spin-down (E_z -H_z) modes. Extracted field and phase distribution are shown in Figure 3.14. The symmetric field profie (Figure 3.14a) indicates the energy degeneracy while the phase distribution (Figure 3.14b) clearly shows the perferred directionality of the spin -up and -down modes respectively.

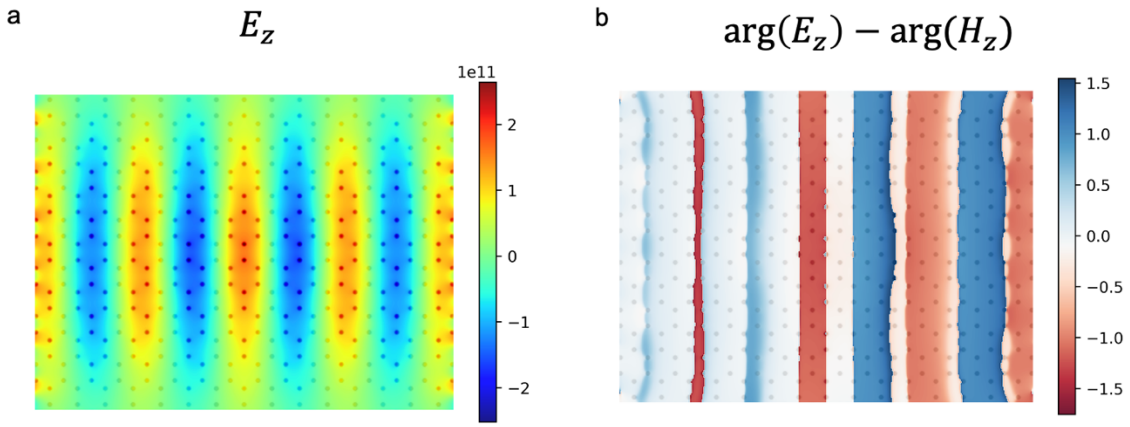

Figure 3.14 (a) E_z field distribution under the excitation of a spinless source in the middle of the simulation region. (b) Arg(E_z) - arg(H_z) phase distribution.

The one-to-one correspondence between the off-diagonal tensor elements and the spin-polarized band splitting endow the underlying system more flexibility. By assigning $\varepsilon_{xz} = -\mu_{xz} \neq 0$, bands around K point now shift along positive and negative k_y (Figure 3.15a). In consequence, the spin-polarized modes with opposite k_y component counter propagate in y direction instead of x (Figure 3.15b). The field and phase information in Figure 3.15c and 3.15d confirm the manipulability and the tunability of the optical spin Hall enabled by Rashba-Dresselhaus SOC.

For further direct imaging and probing of the photonic system with SOC, birefringent dielectrics can be used as the constituting materials for fabricating the photonic crystals. The required off-diagonal permittivity can be achieved by 'tilting' the birefringent crystal before patterning.

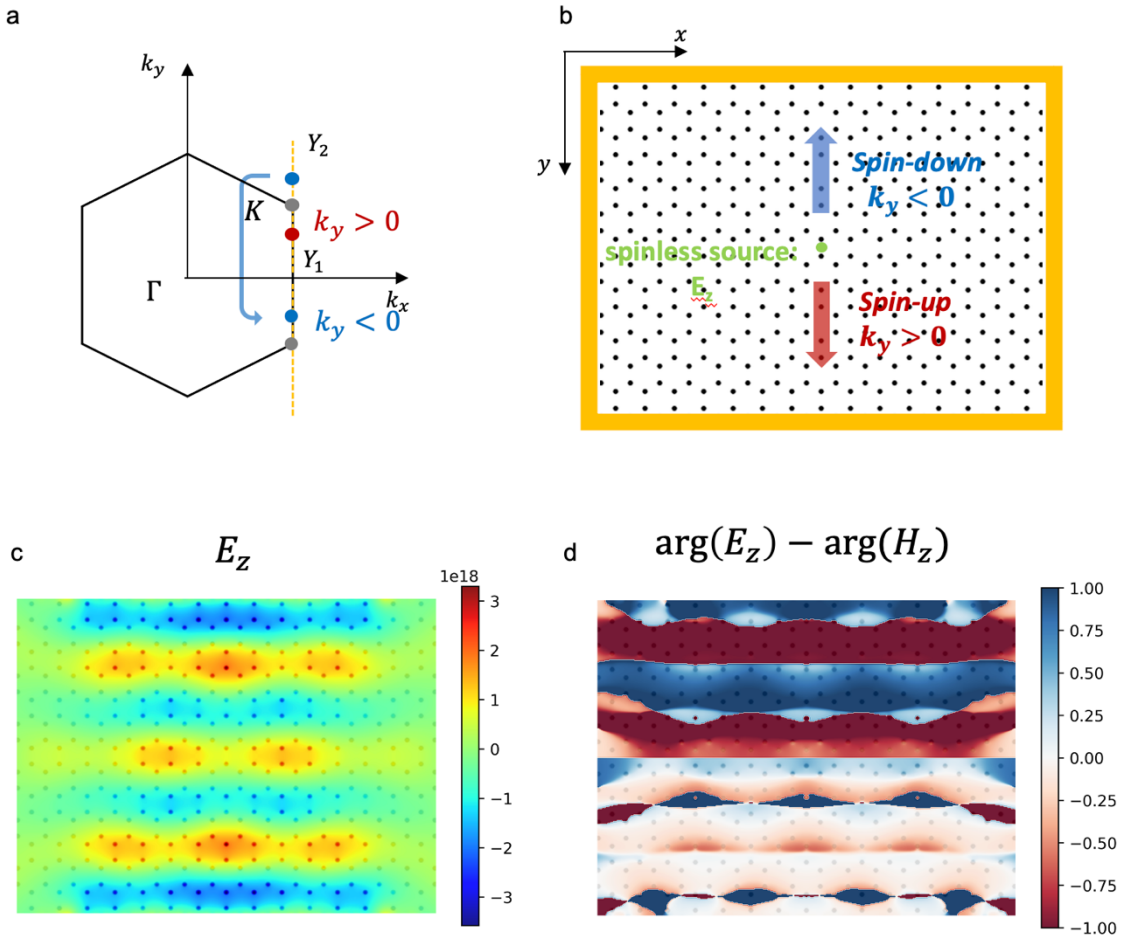

Figure 3.15 (a) Schematics of the splitting in the first Brillouin with nonzero $\varepsilon_{xz}(\mu_{xz})$. (b) Illustration of the counter-propagating spin-polarized bulk waves under a spinless source excitation. (c and d) Simulated field and phase distribution.

In conclusion, we proposed that by adopting anisotropic materialization in a 2D lattice configuration, the induced effective magnetic field will have Rashba-type SOC symmetry. The honeycomb, strained honeycomb and sublattice-symmetry broken honeycomb photonic lattice will reproduce the Bloch states of graphene, monolayer BP and MX respectively. Spin splitting is expected by tilting the anisotropic constitutive parameters with a close correspondence between spin-splitting direction and the tilting angle. Consequently, photonic models of graphene, BP and MX with Rashba-type SOC can be achieved with spin-dependent features same as their solid-states counterparts. Moreover, we will be able to realize a photonic version of spin Hall effect with high flexibility.

Conclusion and outlook

In summary, we started from the general concept of symmetry engineering in two-dimensional systems and discussed in detail the emergent phenomena arising from inversion symmetry breaking. The methodology in changing the symmetry elements of existing materials is generic and provides more flexible platforms for further fundamental physics studies and innovative applications.

In Chapter 1, we demonstrated the twist-angle-dependent SHG in inversion-symmetry-broken tBLGs. The effect of underlying symmetry and electronic structure on SHG response is revealed by polarization measurements and symmetry point group analysis. Strongly coupled bilayer dispersion distinguishes itself from previous nonlinear engineering work based on the fixed susceptibilities.

The direct relation between tensor components and polarization pattern indicates a potential way to probe and characterize the high symmetry axis of tBLG system in a nondestructive manner. Moreover, the inversion symmetry breaking and the existence of chiral tensors imply emerging mechanical properties such as piezoelectricity. The 'twisting' can be achieved artificially during transfer process or naturally occur in material growth. In all these systems, our symmetry analysis applies and we expect more exotic nonlinear behavior from multi-layer twisted vdW materials with more complicated crystal symmetries.

In Chapter 2, we break the inversion symmetry of 2D lattices by utilizing 'tilted' anisotropic materials. Consequently, the induced effective magnetic field will have Rashba-Dresselhaus type SOC symmetry. We further demonstrate the universality by applying it to honeycomb, strained honeycomb and sublattice-symmetry broken honeycomb photonic lattices to reproduce the Bloch states of graphene, monolayer BP and MX respectively Moreover, due to the lifting of degeneracy, edge states on ribbon structure become spin polarized and locked with momentum over a limited range of wavenumbers. A photonic version of spin Hall effect with high flexibility is also demonstrate with counter-propagating spin-polarized waves under the excitation of a spinless source.

For future experimental imaging and characterization of the photonic system with SOC, birefringent dielectrics as the constituting materials can be employed. The required off-diagonal permittivity can be achieved by tilting the birefringent crystal before fabrication. The spin-polarized bulk and edge states achieved here will pave the way for integrated photonic spintronics and communication applications.

Appendix

Local Berry curvature calculations are conducted in MEEP[130–132].

First, we setup the simulation of a triangular lattice with two sublattices in one unit cell. Constitutive parameters are separated into diagonal and off-diagonal parts.

```
geometry_lattice = mp.Lattice(size=mp.Vector3(1, 1),
                              basis1=mp.Vector3(3/2, math.sqrt(3)/2),
                              basis2=mp.Vector3(3/2, -math.sqrt(3)/2))
geometry = [mp.Cylinder(0.1,
center=mp.Vector3(0,0),material=mp.Medium(epsilon_diag=eps_diag,epsilon_offdiag=e
ps_off,mu_diag=mu_diag,mu_offdiag=mu_off)),
            mp.Cylinder(0.1,
center=mp.Vector3(1/3,1/3),material=mp.Medium(epsilon_diag=eps_diag,epsilon_offdia
g=eps_off,mu_diag=mu_diag,mu_offdiag=mu_off))]
```

For the 2D plot of Berry curvature distribution, the first Brillouin zone (BZ) is discretized according to the symmetry of lattice.

```
square_stepx=30
square_stepy=30
all_kpt=[]
for n1 in range(square_stepx):
   for n2 in range(square_stepy):
      #all_kpt.append(mp.Vector3((-0.5+n1/(square_stepy-1))+(-0.5+n2/(square_stepx-
1)),(-0.5+n1/(square_stepy-1))))
      #all_kpt.append(mp.Vector3(n2/(square_stepy-1)-0.25+0.5*n1/(square_stepy-1),-
0.5+n1/(square_stepy-1)))
```

For nondegenerate cases, the local Berry phase is calculated around each plaquette:
$\phi = -Im \log [< u_{k_1}(r)|u_{k_2}(r) >< u_{k_2}(r)|u_{k_3}(r) >< u_{k_3}(r)|u_{k_4}(r) >< u_{k_4}(r)|u_{k_1}(r) >]$
where $u_{k_i}(r)$ is the periodic part of the frequency domain solved Bloch states $E_z(r)$.

The Local Berry curvature calculation repeats for the entire 2D BZ:

```
berryphase=np.zeros((square_stepx-1,square_stepy-1))
for nx in range(square_stepx-1):
   for ny in range(square_stepy-1):
      prod=1+0j
      prod*=np.vdot(np.multiply(eps,Ez_matrix[nx,ny,:,:]),Ez_matrix[nx,ny+1,:,:])
      prod*=np.vdot(np.multiply(eps,Ez_matrix[nx,ny+1,:,:]),Ez_matrix[nx+1,ny+1,:,:])
      prod*=np.vdot(np.multiply(eps,Ez_matrix[nx+1,ny+1,:,:]),Ez_matrix[nx+1,ny,:,:])
      prod*=np.vdot(np.multiply(eps,Ez_matrix[nx+1,ny,:,:]),Ez_matrix[nx,ny,:,:])
      berryphase[nx,ny]=-np.angle(prod)
```

Based on the local Berry curvature calculation, we are able to evaluate the Chern number for a certain band by summing up discrete values. For the cases we studied here, time-reversal symmetry dictates zero total Chern number. However, for the staggered lattice, valley Chern number becomes nonzero and can be obtained by integrating over half of first BZ.

```
Chern=sum(sum(berryphase))/2/np.pi
```

For the calculation of Wilson loop or Zak phase for ribbon structure, the first BZ is discretized in a similar way. The inner product is conducted only along k_x(k_y) direction and the one-dimensional plot is obtained with k_y(k_x) being the horizontal axis.

```
Wilsonloop=np.zeros(square_stepy)
for nx in range(square_stepy):
    prod=1+0j
    for ny in range(square_stepx-1):
        prod*=np.vdot(np.multiply(eps,Ez_matrix[nx,ny,:,:]),Ez_matrix[nx,ny+1,:,:])
    Wilsonloop[nx]=-np.angle(prod)/2/np.pi
```

Bibliography

1. Geim, A. K. & Grigorieva, I. V. Van der Waals heterostructures. *Nature* **499**, 419–425 (2013).
2. Liu, Y. *et al.* Van der Waals heterostructures and devices. *Nat. Rev. Mater.* **1**, 16042 (2016).
3. Novoselov, K. S., Mishchenko, A., Carvalho, A. & Castro Neto, A. H. 2D materials and van der Waals heterostructures. *Science* **353**, aac9439 (2016).
4. Jin, C. *et al.* Ultrafast dynamics in van der Waals heterostructures. *Nat. Nanotechnol.* **13**, 994–1003 (2018).
5. Cao, Y. *et al.* Unconventional superconductivity in magic-angle graphene superlattices. *Nature* **556**, 43–50 (2018).
6. Cao, Y. *et al.* Correlated insulator behaviour at half-filling in magic-angle graphene superlattices. *Nature* **556**, 80–84 (2018).
7. Nuckolls, K. P. *et al.* Strongly correlated Chern insulators in magic-angle twisted bilayer graphene. *Nature* **588**, 610–615 (2020).
8. Sharpe, A. L. *et al.* Emergent ferromagnetism near three-quarters filling in twisted bilayer graphene. *Science* **365**, 605–608 (2019).
9. Du, L. *et al.* Engineering symmetry breaking in two-dimensional layered materials. 35.
10. Zhang, Y. *et al.* Direct observation of a widely tunable bandgap in bilayer graphene. *Nature* **459**, 820–823 (2009).
11. Weitz, R. T., Allen, M. T., Feldman, B. E., Martin, J. & Yacoby, A. Broken-Symmetry States in Doubly Gated Suspended Bilayer Graphene. *Science* **330**, 812–816 (2010).
12. Shimazaki, Y. *et al.* Generation and detection of pure valley current by electrically induced Berry curvature in bilayer graphene. *Nat. Phys.* **11**, 1032–1036 (2015).
13. Brun, S. J. & Pedersen, T. G. Intense and tunable second-harmonic generation in biased bilayer graphene. *Phys. Rev. B - Condens. Matter Mater. Phys.* **91**, (2015).
14. Sui, M. *et al.* Gate-tunable topological valley transport in bilayer graphene. *Nat. Phys.* **11**, 1027–1031 (2015).
15. Castro, E. V. *et al.* Biased Bilayer Graphene: Semiconductor with a Gap Tunable by the Electric Field Effect. *Phys. Rev. Lett.* **99**, 216802 (2007).
16. Yankowitz, M., Ma, Q., Jarillo-Herrero, P. & LeRoy, B. J. van der Waals heterostructures combining graphene and hexagonal boron nitride. *Nat. Rev. Phys.* **1**, 112–125 (2019).
17. Gorbachev, R. V. *et al.* Detecting topological currents in graphene superlattices. *Science* **346**, 448–451 (2014).
18. Xiao, D., Yao, W. & Niu, Q. Valley-Contrasting Physics in Graphene: Magnetic Moment and Topological Transport. *Phys. Rev. Lett.* **99**, 236809 (2007).
19. Stepanov, E. A. *et al.* Direct Observation of Incommensurate–Commensurate Transition in Graphene-hBN Heterostructures via Optical Second Harmonic Generation. *ACS Appl. Mater. Interfaces* **12**, 27758–27764 (2020).
20. Dong, J.-W., Chen, X.-D., Zhu, H., Wang, Y. & Zhang, X. Valley photonic crystals for control of spin and topology. *Nat. Mater.* **16**, 298–302 (2017).
21. Xue, H., Yang, Y. & Zhang, B. Topological Valley Photonics: Physics and Device Applications. *Adv. Photonics Res.* **2**, 2100013 (2021).
22. Chen, X.-D., Zhao, F.-L., Chen, M. & Dong, J.-W. Valley-contrasting physics in all-dielectric photonic crystals: Orbital angular momentum and topological propagation. *Phys. Rev. B* **96**, 020202 (2017).

23. Song, D. *et al.* Unveiling pseudospin and angular momentum in photonic graphene. *Nat. Commun.* **6**, 6272 (2015).
24. Ribeiro-Palau, R. *et al.* Twistable electronics with dynamically rotatable heterostructures. *Science* **361**, 690–693 (2018).
25. Yang, F. *et al.* Tunable Second Harmonic Generation in Twisted Bilayer Graphene. *Matter* **3**, 1361–1376 (2020).
26. Du, L., Dai, Y. & Sun, Z. Twisting for Tunable Nonlinear Optics. *Matter* **3**, 987–988 (2020).
27. Hsu, W.-T. *et al.* Second Harmonic Generation from Artificially Stacked Transition Metal Dichalcogenide Twisted Bilayers. *ACS Nano* **8**, 2951–2958 (2014).
28. Carr, S. *et al.* Twistronics: Manipulating the electronic properties of two-dimensional layered structures through their twist angle. *Phys. Rev. B* **95**, 075420 (2017).
29. Scuri, G. *et al.* Electrically Tunable Valley Dynamics in Twisted WSe 2 / WSe 2 Bilayers. *Phys. Rev. Lett.* **124**, 217403 (2020).
30. Son, J., Kim, K.-H., Ahn, Y. H., Lee, H.-W. & Lee, J. Strain Engineering of the Berry Curvature Dipole and Valley Magnetization in Monolayer MoS 2. *Phys. Rev. Lett.* **123**, 036806 (2019).
31. Guinea, F., Katsnelson, M. I. & Geim, A. K. Energy gaps and a zero-field quantum Hall effect in graphene by strain engineering. *Nat. Phys.* **6**, 30–33 (2010).
32. Levy, N. *et al.* Strain-Induced Pseudo–Magnetic Fields Greater Than 300 Tesla in Graphene Nanobubbles. *Science* **329**, 544–547 (2010).
33. Nandkishore, R. & Levitov, L. Quantum anomalous Hall state in bilayer graphene. *Phys. Rev. B* **82**, 115124 (2010).
34. Bultinck, N., Chatterjee, S. & Zaletel, M. P. Mechanism for Anomalous Hall Ferromagnetism in Twisted Bilayer Graphene. *Phys. Rev. Lett.* **124**, 166601 (2020).
35. Wang, Z., Tang, C., Sachs, R., Barlas, Y. & Shi, J. Proximity-Induced Ferromagnetism in Graphene Revealed by the Anomalous Hall Effect. *Phys. Rev. Lett.* **114**, 016603 (2015).
36. Yu, R. *et al.* Quantized Anomalous Hall Effect in Magnetic Topological Insulators. *Science* **329**, 61–64 (2010).
37. Yankowitz, M. *et al.* Tuning superconductivity in twisted bilayer graphene. *Science* **363**, 1059–1064 (2019).
38. Zou, L., Po, H. C., Vishwanath, A. & Senthil, T. Band structure of twisted bilayer graphene: Emergent symmetries, commensurate approximants, and Wannier obstructions. *Phys. Rev. B* **98**, 085435 (2018).
39. Havener, R. W., Liang, Y., Brown, L., Yang, L. & Park, J. Van Hove Singularities and Excitonic Effects in the Optical Conductivity of Twisted Bilayer Graphene. *Nano Lett.* **14**, 3353–3357 (2014).
40. Li, G. *et al.* Observation of Van Hove singularities in twisted graphene layers. *Nat. Phys.* **6**, 109–113 (2010).
41. Patel, H., Huang, L., Kim, C.-J., Park, J. & Graham, M. W. Stacking angle-tunable photoluminescence from interlayer exciton states in twisted bilayer graphene. *Nat. Commun.* **10**, 1445 (2019).
42. Carozo, V. *et al.* Resonance effects on the Raman spectra of graphene superlattices. *Phys. Rev. B - Condens. Matter Mater. Phys.* **88**, (2013).
43. Kim, C. J. *et al.* Chiral atomically thin films. *Nat. Nanotechnol.* **11**, 520–524 (2016).
44. Patel, H. *et al.* Tunable Optical Excitations in Twisted Bilayer Graphene Form Strongly Bound Excitons. *Nano Lett.* **15**, 5932–5937 (2015).

45. Jorio, A. *et al.* Optical-Phonon Resonances with Saddle-Point Excitons in Twisted-Bilayer Graphene. *Nano Lett.* **14**, 5687–5692 (2014).
46. Yin, X. *et al.* Edge Nonlinear Optics on a MoS $_2$ Atomic Monolayer. *Science* **344**, 488–490 (2014).
47. Li, Y. *et al.* Probing symmetry properties of few-layer MoS2 and h-BN by optical second-harmonic generation. *Nano Lett.* **13**, 3329–3333 (2013).
48. Shan, Y. *et al. Stacking symmetry governed second harmonic generation in graphene trilayers*. http://advances.sciencemag.org/ (2018).
49. Dean, J. J. & van Driel, H. M. Second harmonic generation from graphene and graphitic films. *Appl. Phys. Lett.* **95**, 261910 (2009).
50. Avetissian, H. K., Mkrtchian, G. F., Batrakov, K. G., Maksimenko, S. A. & Hoffmann, A. Multiphoton resonant excitations and high-harmonic generation in bilayer graphene. *Phys. Rev. B - Condens. Matter Mater. Phys.* **88**, (2013).
51. Wu, S. *et al.* Quantum-Enhanced Tunable Second-Order Optical Nonlinearity in Bilayer Graphene. *Nano Lett.* **12**, 2032–2036 (2012).
52. Boyd, R. W. (2008). Nonlinear.Optics, 3rd Edition (Academic Press).
53. Psilodimitrakopoulos, S. *et al.* Twist Angle mapping in layered WS2 by Polarization-Resolved Second Harmonic Generation. *Sci. Rep.* **9**, (2019).
54. Pizzocchero, F. *et al.* The hot pick-up technique for batch assembly of van der Waals heterostructures. *Nat. Commun.* **7**, (2016).
55. Wang, X. H. *et al.* Vector model for polarized second-harmonic generation microscopy under high numerical aperture. *J. Opt. Pure Appl. Opt.* **12**, (2010).
56. Malard, L. M., Alencar, T. V., Barboza, A. P. M., Mak, K. F. & De Paula, A. M. Observation of intense second harmonic generation from MoS2 atomic crystals. *Phys. Rev. B - Condens. Matter Mater. Phys.* **87**, (2013).
57. Trolle, M. L., Seifert, G. & Pedersen, T. G. Theory of excitonic second-harmonic generation in monolayer MoS2. *Phys. Rev. B - Condens. Matter Mater. Phys.* **89**, (2014).
58. Lui, C. H., Mak, K. F., Shan, J. & Heinz, T. F. Ultrafast Photoluminescence from Graphene. *Phys. Rev. Lett.* **105**, 127404 (2010).
59. Liu, W.-T. *et al.* Nonlinear broadband photoluminescence of graphene induced by femtosecond laser irradiation. *Phys. Rev. B* **82**, 081408 (2010).
60. Alencar, T. V. *et al.* Twisted bilayer graphene photoluminescence emission peaks at van Hove singularities. *J. Phys. Condens. Matter* **30**, (2018).
61. Koshino, M. & Moon, P. Electronic Properties of Incommensurate Atomic Layers. *J. Phys. Soc. Jpn.* **84**, 121001 (2015).
62. Verbiest, T. *et al.* Strong Enhancement of Nonlinear Optical Properties Through Supramolecular Chirality. *Science* **282**, 913–915 (1998).
63. Verbiest, T. *et al.* Second-Order Nonlinear Optical Properties of Highly Symmetric Chiral Thin Films. *Langmuir* **17**, 4685–4687 (2001).
64. Dailey, C. A., Burke, B. J. & Simpson, G. J. The general failure of Kleinman symmetry in practical nonlinear optical applications. *Chem. Phys. Lett.* **390**, 8–13 (2004).
65. Song, W., Guo, G.-Y., Huang, S., Yang, L. & Yang, L. First-principles Studies of Second-Order Nonlinear Optical Properties of Organic-Inorganic Hybrid Halide Perovskites. *Phys. Rev. Appl.* **13**, 014052 (2020).
66. Kang, H., Jia, B. & Gu, M. Polarization characterization in the focal volume of high numerical aperture objectives. *Opt. Express* **18**, 10813 (2010).

67. Yew, E. Y. S. & Sheppard, C. J. R. Effects of axial field components on second harmonic generation microscopy. 8 (2006).
68. Wang, G. *et al.* In-Plane Propagation of Light in Transition Metal Dichalcogenide Monolayers: Optical Selection Rules. *Phys. Rev. Lett.* **119**, (2017).
69. Sato, K., Saito, R., Cong, C., Yu, T. & Dresselhaus, M. S. Zone folding effect in Raman G - band intensity of twisted bilayer graphene. *Phys. Rev. B* **86**, 125414 (2012).
70. Eliel, G. S. N. *et al.* Intralayer and interlayer electron-phonon interactions in twisted graphene heterostructures. *Nat. Commun.* **9**, (2018).
71. Patankar, S. *et al.* Resonance-enhanced optical nonlinearity in the Weyl semimetal TaAs. *Phys. Rev. B* **98**, 165113 (2018).
72. Wang, G. *et al.* Giant Enhancement of the Optical Second-Harmonic Emission of WSe 2 Monolayers by Laser Excitation at Exciton Resonances. *Phys. Rev. Lett.* **114**, 097403 (2015).
73. Erley, G. & Daum, W. Silicon interband transitions observed at Si (100) − S i O 2 interfaces. *Phys. Rev. B* **58**, R1734–R1737 (1998).
74. Suzuki, T. Surface-state transitions of Si„111…-7Ã7 probed using nonlinear optical spectroscopy. 4.
75. Liu, Y. *et al.* Helical van der Waals crystals with discretized Eshelby twist. *Nature* **570**, 358–362 (2019).
76. Aidelsburger, M., Nascimbene, S. & Goldman, N. Artificial gauge fields in materials and engineered systems. *Comptes Rendus Phys.* **19**, 394–432 (2018).
77. Haldane, F. D. M. & Raghu, S. Possible Realization of Directional Optical Waveguides in Photonic Crystals with Broken Time-Reversal Symmetry. *Phys. Rev. Lett.* **100**, 013904 (2008).
78. Wang, Z., Chong, Y. D., Joannopoulos, J. D. & Soljačić, M. Reflection-Free One-Way Edge Modes in a Gyromagnetic Photonic Crystal. *Phys. Rev. Lett.* **100**, 013905 (2008).
79. Wang, Z., Chong, Y., Joannopoulos, J. D. & Soljačić, M. Observation of unidirectional backscattering-immune topological electromagnetic states. *Nature* **461**, 772–775 (2009).
80. Kuhl, U. & Stöckmann, H.-J. Microwave Realization of the Hofstadter Butterfly. *Phys. Rev. Lett.* **80**, 3232–3235 (1998).
81. Ningyuan, J., Owens, C., Sommer, A., Schuster, D. & Simon, J. Time- and Site-Resolved Dynamics in a Topological Circuit. *Phys. Rev. X* **5**, 021031 (2015).
82. Liang, G. Q. & Chong, Y. D. Optical Resonator Analog of a Two-Dimensional Topological Insulator. *Phys. Rev. Lett.* **110**, 203904 (2013).
83. Hafezi, M., Mittal, S., Fan, J., Migdall, A. & Taylor, J. M. Imaging topological edge states in silicon photonics. *Nat. Photonics* **7**, 1001–1005 (2013).
84. Oka, T. & Aoki, H. Photovoltaic Hall effect in graphene. *Phys. Rev. B* **79**, 081406 (2009).
85. Cayssol, J., Dóra, B., Simon, F. & Moessner, R. Floquet topological insulators. *Phys. Status Solidi RRL - Rapid Res. Lett.* **7**, 101–108 (2013).
86. Lindner, N. H., Refael, G. & Galitski, V. Floquet topological insulator in semiconductor quantum wells. *Nat. Phys.* **7**, 490–495 (2011).
87. Rechtsman, M. C. *et al.* Photonic Floquet topological insulators. *Nature* **496**, 196–200 (2013).
88. Whittaker, C. E. *et al.* Optical analogue of Dresselhaus spin–orbit interaction in photonic graphene. *Nat. Photonics* **15**, 193–196 (2021).
89. Nalitov, A. V., Malpuech, G., Terças, H. & Solnyshkov, D. D. Spin-Orbit Coupling and the Optical Spin Hall Effect in Photonic Graphene. *Phys. Rev. Lett.* **114**, 026803 (2015).
90. Khanikaev, A. B. *et al.* Photonic topological insulators. *Nat. Mater.* **12**, 233–239 (2013).

91. Slobozhanyuk, A. P. *et al.* Experimental demonstration of topological effects in bianisotropic metamaterials. *Sci. Rep.* **6**, 22270 (2016).
92. Hafezi, M., Demler, E. A., Lukin, M. D. & Taylor, J. M. Robust optical delay lines with topological protection. *Nat. Phys.* **7**, 907–912 (2011).
93. Gao, F. *et al.* Probing topological protection using a designer surface plasmon structure. *Nat. Commun.* **7**, 11619 (2016).
94. Manchon, A., Koo, H. C., Nitta, J., Frolov, S. M. & Duine, R. A. New perspectives for Rashba spin-orbit coupling. *Nat. Mater.* **14**, 871–882 (2015).
95. Min, H. *et al.* Intrinsic and Rashba spin-orbit interactions in graphene sheets. *Phys. Rev. B - Condens. Matter Mater. Phys.* **74**, (2006).
96. Kochan, D., Irmer, S. & Fabian, J. Model spin-orbit coupling Hamiltonians for graphene systems. *Phys. Rev. B* **95**, 165415 (2017).
97. Dedkov, Yu. S., Fonin, M., Rüdiger, U. & Laubschat, C. Rashba Effect in the Graphene/Ni(111) System. *Phys. Rev. Lett.* **100**, 107602 (2008).
98. Varykhalov, A. *et al.* Electronic and Magnetic Properties of Quasifreestanding Graphene on Ni. *Phys. Rev. Lett.* **101**, 157601 (2008).
99. Ohta, T., Bostwick, A., Seyller, T., Horn, K. & Rotenberg, E. Controlling the Electronic Structure of Bilayer Graphene. *Science* **313**, 951–954 (2006).
100. Kim, J. *et al.* Two-Dimensional Dirac Fermions Protected by Space-Time Inversion Symmetry in Black Phosphorus. *Phys. Rev. Lett.* **119**, (2017).
101. Baik, S. S., Kim, K. S., Yi, Y. & Choi, H. J. Emergence of Two-Dimensional Massless Dirac Fermions, Chiral Pseudospins, and Berry's Phase in Potassium Doped Few-Layer Black Phosphorus. *Nano Lett.* **15**, 7788–7793 (2015).
102. Ahn, J. & Yang, B.-J. Unconventional Topological Phase Transition in Two-Dimensional Systems with Space-Time Inversion Symmetry. *Phys. Rev. Lett.* **118**, 156401 (2017).
103. Plotnik, Y. *et al.* Analogue of Rashba pseudo-spin-orbit coupling in photonic lattices by gauge field engineering. *Phys. Rev. B* **94**, 020301 (2016).
104. Rechcińska, K. *et al.* Engineering spin-orbit synthetic Hamiltonians in liquid-crystal optical cavities. *Science* **366**, 727–730 (2019).
105. Lekenta, K. *et al.* Tunable optical spin Hall effect in a liquid crystal microcavity. *Light Sci. Appl.* **7**, 74 (2018).
106. Kokhanchik, P., Sigurdsson, H., Piętka, B., Szczytko, J. & Lagoudakis, P. G. Photonic Berry curvature in double liquid crystal microcavities with broken inversion symmetry. *Phys. Rev. B* **103**, (2021).
107. Jonathan N. et al. Artificial gauge field and topological phenomena through all-dielectric birefringence. CLEO (2017).
108. Liu, F., Liang, Z. & Li, J. Manipulating Polarization and Impedance Signature: A Reciprocal Field Transformation Approach. *Phys. Rev. Lett.* **111**, 033901 (2013).
109. Liu, F. & Li, J. Gauge Field Optics with Anisotropic Media. *Phys. Rev. Lett.* **114**, 103902 (2015).
110. Lin, Q. & Fan, S. Light Guiding by Effective Gauge Field for Photons. *Phys. Rev. X* **4**, 031031 (2014).
111. Solnyshkov, D. & Malpuech, G. Chirality in photonic systems. *Comptes Rendus Phys.* **17**, 920–933 (2016).
112. Kavokin, A., Malpuech, G. & Glazov, M. Optical spin hall effect. *Phys. Rev. Lett.* **95**, (2005).

113. Trier, F. *et al.* Oxide spin-orbitronics: spin–charge interconversion and topological spin textures. *Nat. Rev. Mater.* (2021) doi:10.1038/s41578-021-00395-9.
114. Bernevig, B. A., Orenstein, J. & Zhang, S.-C. Exact SU(2) Symmetry and Persistent Spin Helix in a Spin-Orbit Coupled System. *Phys. Rev. Lett.* **97**, 236601 (2006).
115. Campbell, D. L., Juzeliūnas, G. & Spielman, I. B. Realistic Rashba and Dresselhaus spin-orbit coupling for neutral atoms. *Phys. Rev. A* **84**, 025602 (2011).
116. Luo, W., Xiao, S., He, Q., Sun, S. & Zhou, L. Photonic Spin Hall Effect with Nearly 100% Efficiency. *Adv. Opt. Mater.* **3**, 1102–1108 (2015).
117. Yin, X., Ye, Z., Rho, J., Wang, Y. & Zhang, X. Photonic Spin Hall Effect at Metasurfaces. *Science* **339**, 1405–1407 (2013).
118. Ezawa, M. Topological origin of quasi-flat edge band in phosphorene. *New J. Phys.* **16**, 115004 (2014).
119. Jung, S. W. *et al.* Black phosphorus as a bipolar pseudospin semiconductor. *Nat. Mater.* **19**, 277–281 (2020).
120. Xia, F., Wang, H., Hwang, J. C. M., Neto, A. H. C. & Yang, L. Black phosphorus and its isoelectronic materials. *Nat. Rev. Phys.* **1**, 306–317 (2019).
121. Rodin, A. S., Gomes, L. C., Carvalho, A. & Castro Neto, A. H. Valley physics in tin (II) sulfide. *Phys. Rev. B* **93**, 045431 (2016).
122. Mella, J. D. & Torres, L. E. F. F. Robustness of spin-polarized edge states in a two-dimensional topological semimetal without inversion symmetry. *Phys. Rev. B* **105**, 075403 (2022).
123. Mak, K. F., Xiao, D. & Shan, J. Light–valley interactions in 2D semiconductors. *Nat. Photonics* **12**, 451–460 (2018).
124. Lee, K. W. & Lee, C. E. Quantum valley Hall effect in wide-gap semiconductor SiC monolayer. *Sci. Rep.* **10**, 5044 (2020).
125. Wu, S. *et al.* Electrical tuning of valley magnetic moment through symmetry control in bilayer MoS2. *Nat. Phys.* **9**, 149–153 (2013).
126. Lee, J., Wang, Z., Xie, H., Mak, K. F. & Shan, J. Valley magnetoelectricity in single-layer MoS2. *Nat. Mater.* **16**, 887–891 (2017).
127. Delplace, P., Ullmo, D. & Montambaux, G. The Zak phase and the existence of edge states in graphene. 14.
128. Nakada, K., Fujita, M., Dresselhaus, G. & Dresselhaus, M. S. Edge state in graphene ribbons: Nanometer size effect and edge shape dependence. *Phys. Rev. B* **54**, 17954–17961 (1996).
129. Kim, M., Jacob, Z. & Rho, J. Recent advances in 2D, 3D and higher-order topological photonics. *Light Sci. Appl.* **9**, 130 (2020).
130. Oskooi, A. F. *et al.* Meep: A flexible free-software package for electromagnetic simulations by the FDTD method. *Comput. Phys. Commun.* **181**, 687–702 (2010).
131. Zhao, R. *et al.* First-principle calculation of Chern number in gyrotropic photonic crystals. *Opt. Express* **28**, 4638 (2020).
132. Maria Blanco de Paz, M. B. *et al.* Tutorial: Computing topological invariants in two-dimensional photonic crystals. 13.